CHALMERS
UNIVERSITY OF TECHNOLOGY

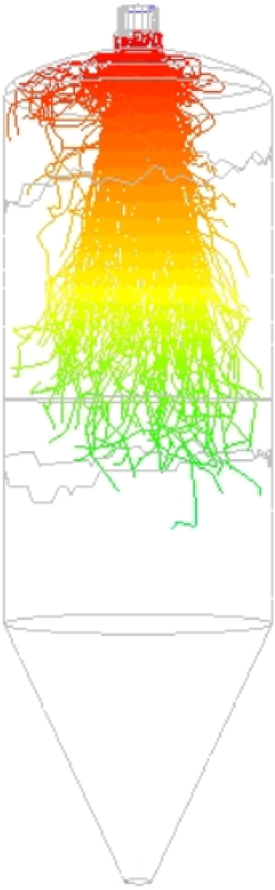

Modeling of multiphase flows in a spray dryer

Master thesis in Innovative and Sustainable Chemical Engineering

Sindhuja Vasudevan

Department of Mechanics and Maritime Sciences
CHALMERS UNIVERSITY OF TECHNOLOGY
Gothenburg, Sweden 2020

Master's thesis 2020

Modeling of multiphase flows in a spray dryer

A CFD methodology to analyse drying behaviour in a spray dryer

SINDHUJA VASUDEVAN

Department of Mechanics and Maritime Sciences
Chalmers University of Technology
Gothenburg, Sweden 2020

Modeling of multiphase flows in a spray dryer
SINDHUJA VASUDEVAN

Master's Thesis 2021:07
Department of Mechanics and Maritime Sciences
Chalmers University of Technology
SE-412 96 Gothenburg
Telephone +46 (0)31-772 1000

Process Engineering, Inhalation Product Development, Pharmaceutical Technology & Development, AstraZeneca, Gothenburg, Sweden

Supervisor: Luis Martin de Juan, Modelling and Simulation, Global Medicines Development, Pharmaceutical Technology & Development, Operations, AstraZeneca, Gothenburg, Sweden
Supervisor: Ingela Niklasson Björn, Process Engineering, Inhalation Product Development, Pharmaceutical Technology & Development, AstraZeneca, Gothenburg, Sweden
Supervisor: Srdjan Sasic, Chalmers University of Technology
Examiner: Srdjan Sasic, Chalmers University of Technology

Cover: Contour showing the distance travelled along the axial direction by the droplets just before they completely dry out.

Typeset in LaTeX
Gothenburg, Sweden 2020

Modeling of multiphase flows in a spray dryer
SINDHUJA VASUDEVAN
Department of Mechanics and Maritime Sciences
Chalmers University of Technology

Abstract

Spray drying is a robust and popular unit operation in the pharmaceutical industry. One of the many applications of this unit operation is the manufacture of dry dosage formulations for nasal or pulmonary delivery. It is important that the generated particles from the spray drying process have certain attributes such as flowability, dispersibility and suitable aerodynamic properties, which depend on the particle design. In order to obtain a suitable particle design, a sound understanding of the particle formation process, which includes the physical and chemical mechanisms that control the drying process, is required. In this thesis, the drying process is studied by modeling with the commercial computational fluid dynamics (CFD) code ANSYS Fluent. This multiphase system which includes a gaseous continuous phase and droplet/particle as the dispersed phase is modeled using an Euler-Lagrangian approach. In Euler-Lagrangian modeling, the fluid phase is modeled as a continuum while for the dispersed phase a large number of individual particles is modeled. The different phases are said to be coupled when there is exchange of momentum, mass and energy between them. The significant presence of exchange of mass and heat between the continuous and dispersed phase indicates that the phases are two-way coupled, i.e., the continuous phase transfers mass and heat to dispersed phase and vice-versa. The effect of turbulence on the dispersed phase is accounted through a turbulent dispersion model. The choice of characteristic parameter of the turbulent dispersion model, i.e., the 'number of tries' is decided based on a sensitivity analysis. This is done by analysing its effect on the residence time distribution of the dispersed phase. Analysis of the drying data obtained from the simulation reveals that the rate of drying of droplets of same initial diameter is different since they follow different trajectories. That is, for droplets of the same initial diameter, the drying rate varies in such a way that the maximum value is around 50% higher than the minimum value. Hence, this implies corresponding variation in solute concentration profile in the droplet and hence, particle structure for particles obtained from droplets of same initial diameter. Additionally, the impact of process operating conditions, especially the mass flow rate of the solution, on the drying rate and hence, the corresponding particle structure is indicated.

Keywords: Spray Drying, Euler-Lagrangian, Discrete Phase Model, Drying Rate

Acknowledgements

I would like to express my gratitude to my supervisor Ingela Niklasson Björn for providing me the opportunity to work on this Master Thesis at AstraZeneca. Her constant support by being in contact on an everyday basis during the tough times of the pandemic and providing valuable comments during the thesis is deeply appreciated. I would like to express my deepest gratitude to my supervisor Luis Martin de Juan for his patient and constant guidance throughout, which was immensely helpful in shaping and completing this thesis. Also, I would like to sincerely thank my examiner, Prof. Srdjan Sasic, for his constant support, insightful comments, and remarks. Many thanks to Johan Remmelgas for his valuable insights. Finally, I would like to extend my gratitude to Karin Sundström and Magnus Svensson for always being there to provide relevant inputs.

This project has been funded by AstraZeneca.

Sindhuja Vasudevan, Gothenburg, October, 2020

Nomenclature

Latin Symbols

A_p	Surface area of droplet/particle, m^2
C_B	Basset/history force coefficient
C_D	Drag coefficient
$c_{p,c}$	Heat capacity of continuous phase at constant pressure, $J/kg-K$
$c_{p,p}$	Heat capacity of droplet/particle at constant pressure, $J/kg-K$
$C_{v,\infty}$	Vapour concentration in the bulk, $kmol/m^3$
$C_{v,s}$	Surface vapour concentration, $kmol/m^3$
C_{vm}	Added/virtual mass coefficient
D_A	Diffusion co-efficient of species A, m^2/s
d_p	Diameter of droplet/particle, m
$d_{p,o}$	Initial diameter of droplet/particle, m
F_p	Hydrodynamic forces acting on all the droplets/particles in the averaging volume, kgm/s^2
g	Acceleration due to gravity, m/s^2
h	Convective heat transfer co-efficient, W/m^2K
h_{lat}	Latent heat of vaporisation, J/kg
k	Turbulent kinetic energy, m^2/s^2
k_c	Mass transfer coefficient, m/s
$k_{eff}^{'}$	Effective thermal conductivity of the mixture, W/mK
$\dot{M}_p$	Mass flow rate of dispersed phase, kg/s
$\dot{m}_p$	Rate of change of mass of droplet/particle, kg/s
$\dot{M}_{p,0}$	Initial mass flow rate of dispersed phase, kg/s
$\dot{m}_{p,k}$	Rate of change of mass of particle k, kg/s
m_p	Mass of droplet/particle, kg

$m_{p,0}$	Initial mass of droplet/particle, kg
$m_{p_{in}}$	Mass of particle on cell entry, kg
$m_{p_{out}}$	Mass of particle on cell exit, kg
Nu_p	Nusselt number of droplet /particle
p	Pressure, Pa
Pr	Prandtl number
q_k	Rate of heat transferred from fluid to droplet k, J/s
Re_p	Reynolds number of droplet/particle
S_A	Source term for species A
S_{energy}	Energy source term, J/m^3s
S_{mass}	Mass source term, kg/m^3s
S_{mom}	Momentum source term, kg/m^2s^2
Sc	Schmidt number
Sh_p	Sherwood number of droplet /particle
St_{mass}	Mass Stokes number
St_{mom}	Momentum Stokes number
T_∞	Temperature in the bulk of the fluid, K
T_c	Temperature of continuous phase, K
T_p	Temperature of droplet/particle, K
$T_{p_{in}}$	Temperature of particle on cell entry, K
$T_{p_{out}}$	Temperature of particle on cell exit, K
T_{ref}	Reference temperature, K
u	Velocity of continuous phase, m/s
$(u_i - v_i)_0$	Initial velocity difference, m/s
u'	Velocity fluctuation, m/s
v	Velocity of droplet/particle, m/s
V_p	Volume of droplet/particle, m^3
V_{avg}	Averaging volume, m^3
$v_{i,k}$	Velocity of particle k, m/s
Z	Total loading

Greek Symbols

α_c	Volume fraction of continuous phase
α_d	Volume fraction of dispersed phase
δV	Sampling volume, m^3
δV_d	Volume of dispersed phase, m^3

ϵ	Turbulent dissipation, m^2/s^3
κ	Evaporation rate, m^2/s
λ	Thermal conductivity, $W/m-K$
μ_c	Viscosity of continuous phase, $kg/m-s$
ω_A	Mass fraction of species A
$\omega_{A,\infty}$	Mass fraction of species A in the freestream
$\omega_{A,s}$	Mass fraction of species A at droplet surface
Φ	Thermal dissipation, J/m^3s
Π_{energy}	Energy coupling parameter
Π_{mass}	Mass coupling parameter
Π_{mom}	Momentum coupling parameter
ρ_c	Density of continuous phase, kg/m^3
ρ_p	Density of dispersed phase, kg/m^3
τ	Shear stress, Pa
τ_f	Characteristic time of the flow field, s
τ_m	Characteristic evaporation time, s
τ_v	Momentum response time, s
ζ	Normally distributed random number

Other Symbols

$\langle\rangle$	Volume-averaged
$\tilde{}$	Mass-averaged

Contents

List of Figures xv

1 Introduction 1
- 1.1 Objectives . . . 3
- 1.2 Limitations . . . 4

2 Case description 5
- 2.1 Drying gas chamber . . . 6
- 2.2 Atomizer . . . 7
- 2.3 Dryer . . . 9

3 Theory 11
- 3.1 Droplet drying . . . 11
- 3.2 Euler-Lagrangian approach . . . 13
  - 3.2.1 Coupling between phases . . . 16
  - 3.2.2 Particle-particle interaction . . . 19
- 3.3 Particle tracking . . . 19
- 3.4 Turbulent dispersion . . . 21
  - 3.4.1 Discrete Random Walk Model . . . 21
- 3.5 Numerical considerations . . . 22
  - 3.5.1 Pressure-based flow solver . . . 22
  - 3.5.2 Coupled algorithm . . . 22
  - 3.5.3 Spatial discretisation schemes . . . 23

4 Methodology 25
- 4.1 Simulation setup . . . 25
  - 4.1.1 Drying gas chamber . . . 25
  - 4.1.2 Atomizer . . . 27
  - 4.1.3 Dryer . . . 30
    - 4.1.3.1 Single phase flow . . . 30
    - 4.1.3.2 Particle tracking . . . 31
    - 4.1.3.3 Other boundary conditions . . . 34
- 4.2 Sensitivity Analysis . . . 35
  - 4.2.1 Turbulence dispersion and number of particles . . . 36
  - 4.2.2 Steady vs Transient . . . 37

5 Results **41**
5.1 Drying gas chamber 41
5.2 Atomizer 43
5.3 Dryer 46
5.3.1 Mesh independence 46
5.3.2 Droplet drying 48

6 Conclusion **59**

Bibliography **61**

A Appendix **I**
A.1 Phase coupling parameter estimation I
A.2 Volume fraction of dispersed phase II
A.3 Estimation of solute concentration in the particle III

List of Figures

1.1 Spray dryer configuration from left to right: co-current, counter-current and mixed flow [6]. 2

2.1 Anhydro MicraSpray 35 alongwith the drying gas chamber and atomizer. 5
2.2 Drying gas chamber 6
2.3 Atomizer 8
2.4 CAD model (from ANSYS) of dryer with drying gas inlet tubes at the top 9

3.1 Schematic of the different drying stages a droplet experiences during the drying process. [12] 12
3.2 Variation of drag coefficient of a sphere with Reynolds number. [17] . 16
3.3 Schematic showing the branching of Lagrangian models. 20

4.1 CAD model (from ANSYS) of drying gas chamber with major dimensions 26
4.2 Polyhedral mesh (from ANSYS) of the drying gas chamber shown on a sectional plane 26
4.3 CAD model (from ANSYS) showing two different isometric views of atomizing gas fluid domain 28
4.4 Sectional view (from ANSYS) showing the atomizer domain meshed with tetrahedral cells and inflation layers at the walls 30
4.5 Sectional view (from ANSYS) showing the dryer domain meshed with tetrahedral cells and inflation layers at the walls 31
4.6 Plot showing Rosin-Rammler curve-fit against the measured droplet size distribution 33
4.7 Classification of dryer walls based on boundary conditions. 35
4.8 Mean residence time of droplets for varying 'number of tries' and 'number of streams' for four representative initial diameters. 37
4.9 Vertex-averaged velocity at several points along y-axis of the dryer plotted over flow time. 38

5.1 Radar plot showing mass flow rate (kg/hr) at the fourteen outlets for three mesh refinements of the drying gas chamber goemetry 41

5.2 Velocity contour plots (from ANSYS) of the drying gas chamber . . . 42
5.3 Atomizer mesh independence study based on mass flow rate at atomizer exit, for an inlet pressure of 2.6 barg. The mesh configuration chosen for further analysis is highlighted. 43
5.4 Contour plots (from ANSYS) for pressure, velocity and static temperature in the atomizer, for the condition of inlet pressure of 2.6 barg. 45
5.5 Vertex-averaged velocity at nine different points at varying heights in the dryer for three mesh refinements plotted for the purpose of mesh independence study. 47
5.6 Mass-weighted residence time distribution of inert droplets introduced in the steady state flow field of the dryer. 48
5.7 Contour plots (from ANSYS) for velocity and static temperature in the dryer, pertaining to 'Case-1' boundary conditions (as detailed in subsubsection 4.1.3.3). 49
5.8 For 'Case-1' boundary conditions :- (a)-(d): Distribution of rate of drying for droplets of different initial diameter; for each initial diameter, the drying data along 400 paths is obtained and plotted. (e): Plot showing spread of drying rate for different initial diameter 51
5.9 For 'Case-1' boundary conditions :- (a)-(d): Distribution of Peclet number for droplets of different initial diameter; for each initial diameter, Peclet number data along 400 paths is obtained and plotted. (e): Plot showing spread of Peclet number for different initial diameter 52
5.10 Solute concentration as a function of radius at high and low drying rate for droplets of initial diameter 6.6 μm and 12.8 μm (obtained from simulations of 'Case-1' boundary conditions). 53
5.11 Solute concentration as a function of radius at high and low drying rate for droplets of initial diameter 25.1 μm and 37.4 μm (obtained from simulations of 'Case-1' boundary conditions). 54
5.12 Comparison of results obtained from simulations with 'Case-1' and 'Case-2' boundary conditions (as detailed in subsubsection 4.1.3.3). . 56
5.13 Contour plot of relative humidity of continuous phase 56
5.14 Tracks of discrete phase coloured based on relative humidity of continuous phase 57

A.1 Contour plot of volume fraction of the discrete phase. III

1

Introduction

Spray drying is a process in which small particles are produced by rapid moisture evaporation from a spray of droplets. This unit operation is especially suitable for handling delicate pharmaceutical and biotechnological products due to its advantages such as its reproducibility, fast drying capability, and short exposure of product to high processing temperatures [1, 2]. It is one of the most promising methods for production of particles with controllable morphology. Morphological control opens up great potential for use in various applications, especially for inhalation products in the pharmaceutical industry [3, 4].

The primary stages in spray drying include atomization, solvent evaporation, and particle collection. The process of atomization is key in determining particle size. Here, the initial liquid/solution is fed into a specific atomization equipment for conversion to droplet form. This can be achieved with several types of driving force such as pressure, centrifugal, electrostatic, and ultrasonic energy, and the choice depends on the required droplet size distribution, system to be atomized and capacity requirements. Thus, several atomizers are available like rotary atomizers (includes disk, vanes, cups), two-fluid nozzle (includes external and internal) and pneumatic or pressure nozzles, to name a few. Solvent drying is the step that converts the droplets from the atomizer to particles. Typically, the droplets from the atomizer enter a chamber, via the flow of carrier gas, where solvent evaporation takes place, while the desired non-evaporating components remain in the final product. The carrier gas generally used is either air, inert gas or steam, and depends on the chemical component type, sensitivity of the particle and the solvent to the gas, as well as economical reasons. The flow configuration in this chamber can be co-current, counter-current or mixed flow as shown in Figure 1.1. Finally, in the particle collection step, the dried particles are collected using equipment such as a cyclone filter, a filter bag, an electric field precipitator or just gravity, if the particles are large enough. [3, 5]

Drying, in general, can appear deceptively simple when in reality it involves complex multi-scale and multi-physics transformations. Drying involves the presence of multiphase transport phenomena between drying agent, droplets and particles which occur on multiple scales, in combination with external and internal heat and mass transfer in each phase. Hence, study of drying supported only by experimental measurements is insufficient. Thus, modeling the process helps in better understanding of the physical processes, predicting parametric behaviour, and optimizing the energy consumption of spray drying. [1, 2]

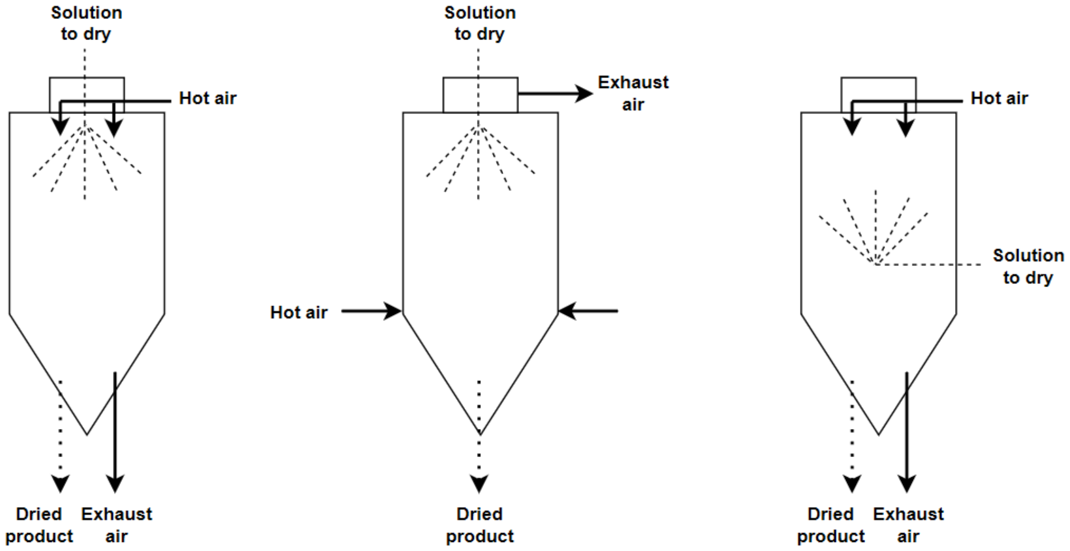

Figure 1.1: Spray dryer configuration from left to right: co-current, counter-current and mixed flow [6].

Different modeling tools offer varying predictive capabilities and accuracy and hence, differ in implementation difficulty and requirement of computational resources. The 'zero-dimensional' approach simulates the drying process using overall heat and mass balances to predict gas temperature, gas humidity and product moisture content at the outlet of the dryer. In this approach, drying chambers are mostly treated as well-mixed reactors and the spray dryer is considered a 'black box' since the focus is on macroscopic properties [2, 7]. In the 1-D transport-based model, apart from the execution of mass, momentum and heat balances, the drying kinetics is also incorporated, thus, allowing the prediction of drying-rate profiles and some degree of understanding and prediction of particle structural changes resulting from drying. The ability of the model to predict temperature and moisture profiles of the gas and droplet/particle and in some cases, the structure profile of droplet/particle is helpful in further predicting various thermo-physical properties and quality parameters of the product [7]. Despite its advantages over simpler models, 1-D models require as input residence time distribution data that has to be obtained experimentally or via more advance modeling capability. This model capability cannot be used to understand the impact of drying design on particle attributes on its own. Also, they will fail to understand some of the phenomena at meso and micro scale such as impact of turbulence arising from non-uniform, swirling processing and atomizing gas which can influence the accuracy of prediction of powder solvent content. To overcome this, 2D and 3D transport-based models which consist of a set of highly complex non-linear Partial Differential Equations (PDEs) need to be solved. Additionally, these multi-dimensional models are well-suited for lab-scale dryers(which have a Height:Diameter $>$ 2:1) where complexity of flow patterns is greater than in tall-form dryers (which have a Height:Diameter > 5:1). [2, 8]

Modeling of spray dryers can be implemented to address a variety of key issues depending on the final product. In the pharmaceutical industry, especially in the manufacture of dry dosage forms for nasal or pulmonary delivery, it is important that the particles have adequate powder flow properties, dispersibility and suitable aerodynamic properties. There is, thus, a requirement to design complex particles such as hollow, low density particles with controlled surface morphology or particles with functional layers. In some cases, it is desirable to control the spatial distribution of components within the particle in order to improve the performance of inhalation products. Successful particle engineering requires a sound understanding of particle formation process which includes the physical and chemical mechanisms that control the drying process [4, 9]. Modeling can predict gas-flow patterns and particle trajectories enabling the reconstruction of particle history in a dryer. The resulting residence times and drying history of particles enable better understanding of product properties and how they depend on process parameters [10].

The thesis is divided into six chapters. The motivation and a broad methodology path is introduced in this chapter. Chapter 2 describes the case under consideration. The theoretical background of the drying model and the numerical models is covered in Chapter 3. The methodology and sensitivity analysis for various model parameters is described in Chapter 4 and the mesh independence study and results are presented in Chapter 5. Finally, conclusions and discussions on the scope for future investigations are included in Chapter 6. Additional information and results are included in the Appendix.

1.1 Objectives

This thesis aims to develop a model for a lab-scale spray dryer 'Anhydro MicraSpray 35' which is used to produce products for inhalation purposes. As mentioned above, since the study of attributes on a particle level is important for inhalation products and also considering the small-scale of dryer, a multi-dimensional CFD-based methodology is adopted. The objectives of the CFD model are:

- to predict the velocity and temperature profile of the drying gas(continuous phase) and the drying rate of the droplets(dispersed phase),
- to analyse the effect of drying rate on the solute concentration profile in the droplet and predict the effect of process operating conditions on the drying rate.

Here, the continuous phase is modeled in an Eulerian frame and the dispersed phase is tracked in a Lagrangian frame. This is achieved with the Discrete Parcel Method. Since the boundary conditions greatly influence the model, the different components upstream of the dryer body such as the drying gas geometry and the atomizer have also been modeled.

1.2 Limitations

The spray dryer under consideration in this thesis is located in a lab which conforms to GMP standards, due to which experimental data available is scarce. For this reason, no validation could be performed as the corresponding experimental data is not available. The computational resource and available time is also limited, for which reason only steady-state simulations are performed.

2

Case description

The lab-scale spray dryer modeled in this thesis is the ’Anhydro MicraSpray 35 (MS 35)’ from SPX FLOW and is shown in Figure 2.1. The different domains that are modeled are:

- single phase flow in the *drying gas chamber*,
- single phase compressible flow in the *atomizer*,
- multiphase flow including momentum, heat and mass transfer in the *dryer*.

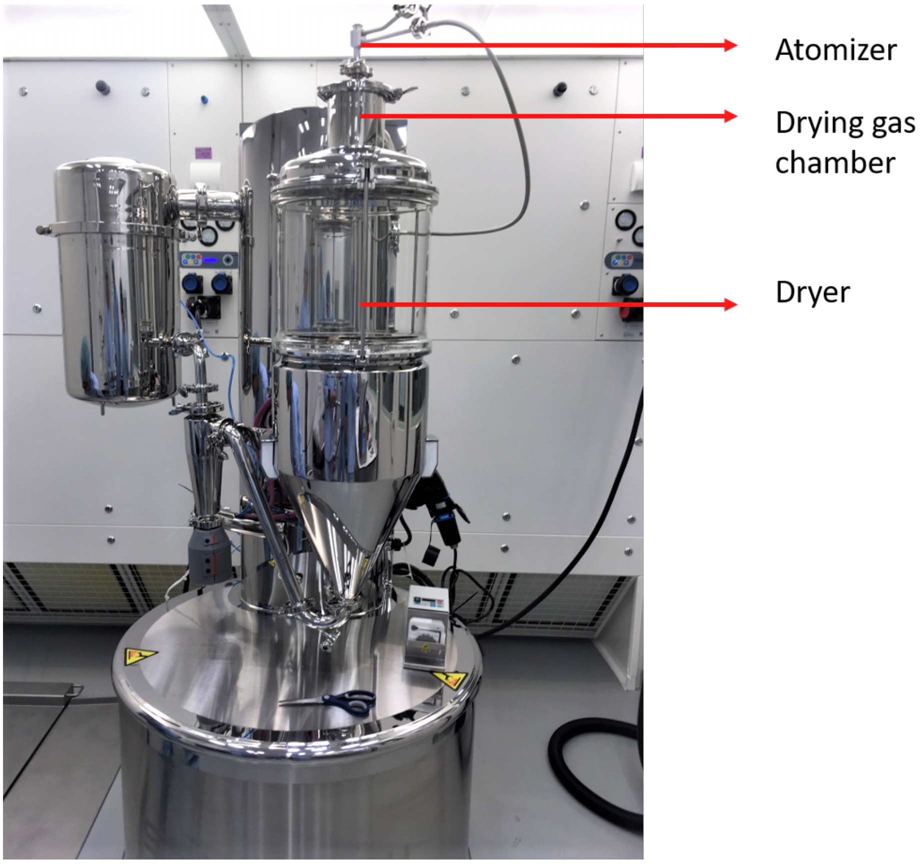

Figure 2.1: Anhydro MicraSpray 35 alongwith the drying gas chamber and atomizer.

The drying gas chamber and the atomizer are modeled to obtain the right boundary conditions to set up the critical system that is the dryer, where the droplet drying occurs. The droplet initial size distribution are obtained from atomization experiments. A detailed description of each of the parts is given below.

2.1 Drying gas chamber

The drying gas chamber refers to the geometry in which the drying gas enters through a cylindrical pipe into a cylindrical chamber which is positioned perpendicular to the inlet pipe. The gas moves up in the chamber, flows through a funnel-like structure and is distributed among fourteen cylindrical tubes before entering the dryer part. The gas inlet and outlet along with a schematic of the flow is depicted in Figure 2.2.

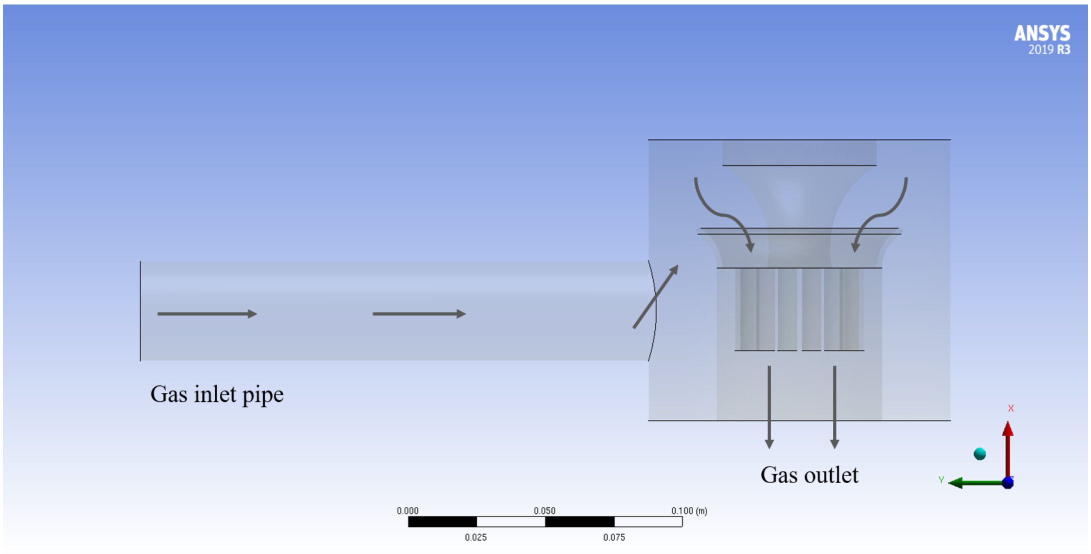

(a) Front view of CAD model (from ANSYS)

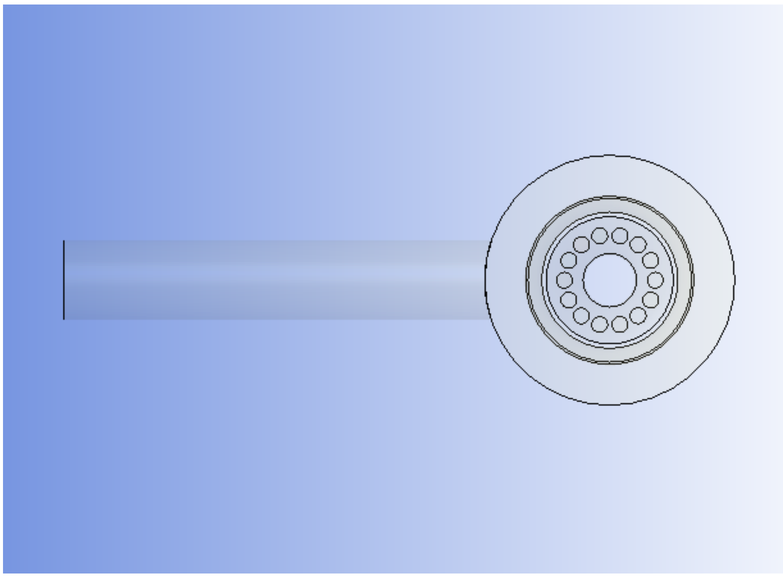

(b) Bottom view of CAD model (from ANSYS)

Figure 2.2: Drying gas chamber

2.2 Atomizer

An atomizer is used to produce fine droplets of the injected solution which are then dried to form particles. For this purpose, a Model 970 Form S1 two-substance nozzle from Schlick is used and is shown in Figure 2.3a. As the name suggests, two substances namely the atomizing gas and the liquid solution flow through different enclosures of the atomizer. The atomizer, thus has two inlets, each for atomizing gas and liquid solution and two outlets, each for atomizing gas ans liquid solution. The liquid passes through the innermost cylinder while the pressurised gas flows through an annular cylinder surrounding the liquid shaft. This gas path has incremental contractions which increase the velocity of the gas. The high speed gas cuts through the liquid sheets exiting from the nozzle thus, resulting in atomized droplets. The flow rate of the atomizing gas for a given pressure can be varied by changing the opening position of what is called an air cap. In this model, the atomizer with air-cap position '5' is used. It is worth mentioning that the atomizer in use in the lab is a slightly modified version and includes a 200 mm shaft through which the fluids flow, and it is this modified version that is modeled. A CAD model of the atomizer is shown in Figure 2.3b. The atomizer model involves modeling of only the atomizing gas flow, and does not include simulation of the atomization process itself.

(a) Model 970 Form S1 Schlick nozzle as shown in product catalogue

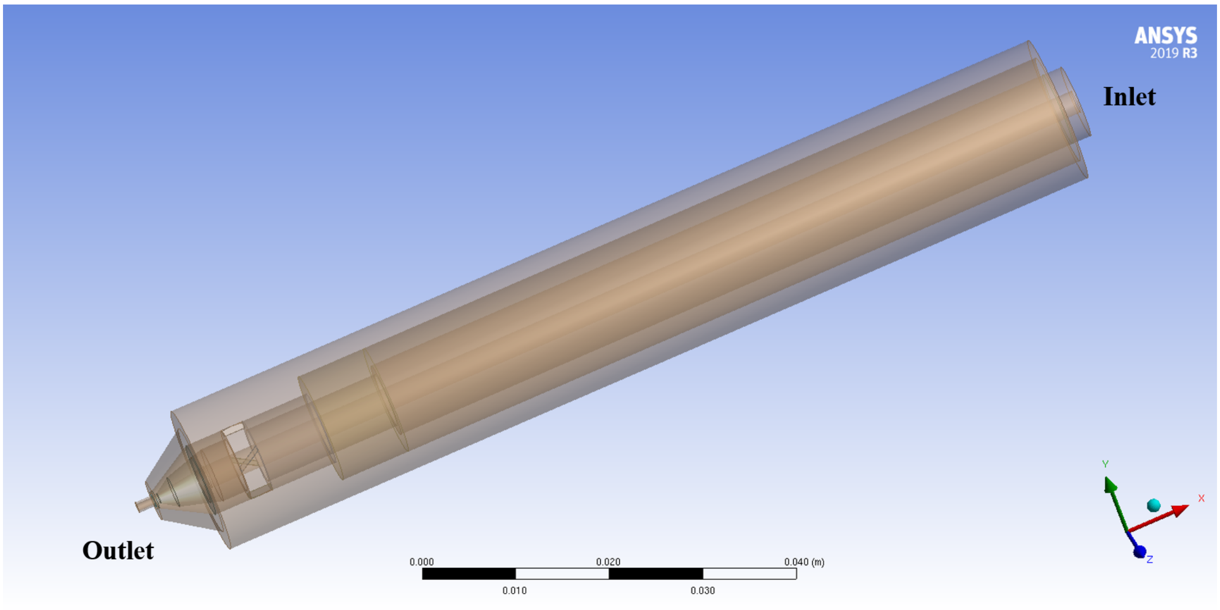

(b) CAD model (from ANSYS) of modified version of Model 970 Form S1 Schlick nozzle

Figure 2.3: Atomizer

2.3 Dryer

The dryer is a cylinder-on-cone configuration as shown in Figure 2.4. The inlet tubes to the tower are included in both the drying gas chamber and the dryer so that the inlet boundary condition is sufficiently far upstream not to influence the flow in the dryer. The sprayed droplets and drying gas flow co-currently with respect to each other and exit through the bottom outlet. The dryer has a height-to-diameter ratio of about 3:1.

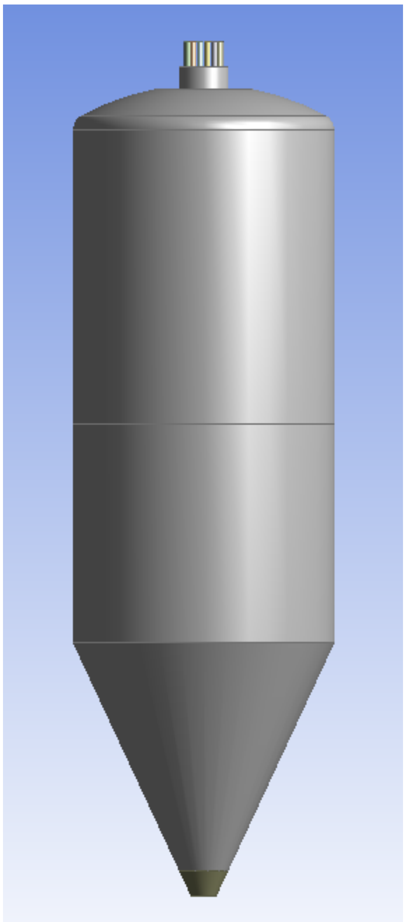

Figure 2.4: CAD model (from ANSYS) of dryer with drying gas inlet tubes at the top

3

Theory

Multiphase flows are characterised by the simultaneous presence of different interacting phases, such as solid, liquid or gas, in a domain of interest. Different modeling techniques exist and the choice mostly depends on the physical process and specification of flow in the system. Modeling of dispersed multiphase flows is commonly described by two approaches namely the Euler-Euler and the Euler-Lagrangian approaches. In the Euler-Euler approach, both the continuous and dispersed phases are solved for in Eulerian refernce frame and are considered as interpenetrating continua. Hence, the properties of the dispersed phase are considered as continuous properties and are obtained through averaging over the control volumes. This approach is preferable for large systems with dense dispersed phase flow. On the other hand, the Euler-Lagrangian approach takes into account the discrete nature of the individual particles. The dispersed phase is solved in a Lagrangian reference frame using the Newton's law of motion, whereas the continuous phase is solved in an Eulerian reference frame. In this study, the Eulerian-Lagrangian approach is used to model the spray dryer since it is more suitable for less dense flows. The 'Discrete Phase Model' implemented in the commercial code ANSYS Fluent is used for this purpose.

In this chapter, the droplet/particle drying mechanism and the corresponding governing equations is presented followed by a detailed description of the Eulerian-Lagrangian approach, the sub-model of turbulent dispersion and the numerical methods used in the modeling of the system. Description of symbols appearing in sub-models and source terms in governing equations, which require further explanation, have been repeated in the text in addition to the nomenclature section. In other cases, the reader is referred to the nomenclature section.

3.1 Droplet drying

The mechanism of drying of sprayed droplets depends on the particle properties and drying conditions. The different stages that are relevant to simulate drying kinetics and morphology evolution of the current system are listed below [11, 12]:

- The initial stage is characterised by the evolution of droplet surface temperature from the initial temperature to the wet bulb temperature and is referred to as the *induction period*. The wet-bulb temperature is attained when the droplet surface gets saturated with the volatile solvent.
- The *constant drying rate period* is said to occur when the droplet surface is

saturated with volatile solvent, and the droplet temperature remains constant at the wet bulb temperature. The drying rate is controlled by external heat and mass transfer rates between the droplet and drying medium. During this stage, the droplet shrinks according to D^2 law which states that the square of the droplet diameter varies linearly with time. Here, the external heat and mass transfer rates between the droplet and the drying medium are balanced.

- When the droplet surface is not saturated anymore, and the drying is controlled by internal mass transfer of the volatile solvent to the surface, then the droplet is said to be in *falling rate period*. The droplet diameter remains constant or presents a relatively small shrinkage due to the formation of a shell or crust at the droplet surface. The reduction in evaporation rate leads to an increase in droplet temperature.
- Once the volatile solvent is completely removed, the temperature of the droplet evolves to the temperature of the drying medium until equilibrium is reached.

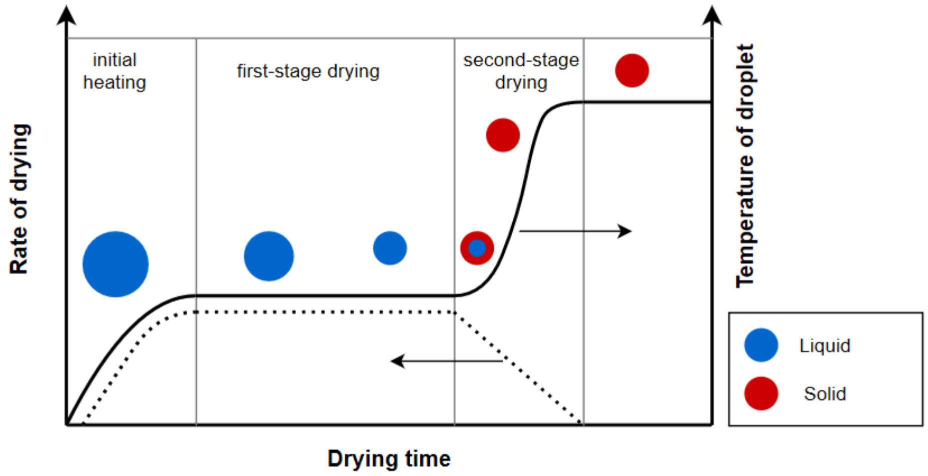

Figure 3.1: Schematic of the different drying stages a droplet experiences during the drying process. [12]

Among the two main stages of drying namely the constant drying rate period (first-stage) and falling rate period (second-stage), for the spray dryer system under consideration, the amount of solvent removed is higher in the first-stage of drying than that in the second-stage. In other words, the amount of solvent removed during the first stage of drying is more than 80% of the total mass of water initially present. Additionally, the composition on the surface of the particle will be controlled by the mechanism of drying during the first stage period. This is because, as solvent evaporation takes place from the surface of the droplet, the solute concentration at the surface increases, and the growing concentration gradient causes a diffusional solute flux away from the droplet surface towards the center of the droplet [12]. Hence, only the first stage of drying, that is critical for this study, is accounted in the current model.

In the first stage of drying, the evaporation of solvent depends on the vapour concentration on the surface and the vapour concentration in the bulk, and the drying rate for a single droplet/particle is given by [1, 13]:

$$\dot{m}_p = \frac{dm_p}{dt} = A_p k_c (C_{v,s} - C_{v,\infty}) \tag{3.1}$$

where the mass transfer co-efficient, k_c, is calculated from the Ranz-Marshall correlation [15]:

$$Sh_p = \frac{k_c d_p}{D_A} = 2 + 0.6 Re_p^{1/2} Sc^{1/3} \tag{3.2}$$

The change in temperature of the droplet/particle with time is the effect of

- heat transfer between particle and the surrounding fluid due to convection, and
- rate of change of energy in the particle due to phase change.

For droplet initial diameters less than 0.25 mm (250 μm) and ambient temperatures less than 750 ^oC (1023 K), the effect of thermal radiation is negligible [14]. Overall, this can be summarised by the following energy balance:

$$m_p c_{p,p} \frac{dT_p}{dt} = h A_p (T_\infty - T_p) - \frac{dm_p}{dt} h_{lat} \tag{3.3}$$

An important assumption with regards to Equation 3.3 is that the inner thermal resistance of particles can be neglected and the temperature is uniform within the particle. This can be quantified using the Biot number(Bi) which is the ratio of heat transfer resistance inside of a body to the resistance at the surface of the body. The above assumption is true when Bi « 1, which is the case in the current system.

The convective heat transfer co-efficient, h, is calculated from the Ranz-Marshall correlation [15]:

$$Nu_p = \frac{h d_p}{\lambda} = 2 + 0.6 Re_p^{1/2} Pr^{1/3} \tag{3.4}$$

In Fluent, the mass transfer in the first stage of drying is implemented through the 'diffusion-controlled' model which models the rate of vaporization to be governed by gradient diffusion. The heat transfer is implemented through the same energy balance as in Equation 3.3. [21]

3.2 Euler-Lagrangian approach

Modeling of the continuous phase in the Eulerian framework requires solving the balance equation of a certain property being transported. This balance equation is written for an Eulerian control volume which is fixed in space and allows for flow through its faces. The balance equations for mass, momentum, energy and species in tensor form for the continuous phase is given below [17]:

$$\frac{\partial(\alpha_c\langle\rho_c\rangle)}{\partial t}+\frac{\partial(\alpha_c\langle\rho_c\rangle\tilde{u_i})}{\partial x_i}=S_{mass} \tag{3.5}$$

$$\begin{aligned}\frac{\partial(\alpha_c\langle\rho_c\rangle\tilde{u_i})}{\partial t}+\frac{\partial(\alpha_c\langle\rho_c\rangle\tilde{u_i}\tilde{u_j})}{\partial x_j}&=-\frac{\partial\langle p\rangle}{\partial x_i}+\frac{\partial\langle\tau_{ij}\rangle}{\partial x_j}+\langle\rho_c\rangle\alpha_c g_i\\&\quad-\frac{\partial}{\partial x_j}(\alpha_c\langle\rho_c u_i'u_j'\rangle)-\frac{1}{V_{avg}}F_p+S_{mom}\end{aligned} \tag{3.6}$$

$$\frac{\partial(\alpha_c\langle\rho_c\rangle c_{p,c}\langle T_c\rangle}{\partial t}+\frac{\alpha_c\langle\rho_c\rangle\tilde{u_i}c_{p,c}\langle T_c\rangle)}{\partial x_i}=c_{p,c}T_pS_{mass}+\alpha_c\langle\Phi\rangle+\frac{\partial}{\partial x_i}(\alpha_c k_{eff}^{'}\frac{\partial\langle T_c\rangle}{\partial x_i})+S_{energy} \tag{3.7}$$

$$\frac{\partial(\alpha_c\langle\rho_c\rangle\langle\omega_A\rangle)}{\partial t}+\frac{\partial(\langle\omega_A\rangle\langle\rho_c\rangle\alpha_c\tilde{u_i})}{\partial x_j}=\frac{\partial}{\partial x_i}(\alpha_c\langle\rho_c\rangle D_A\frac{\partial\omega_A}{\partial x_i})+S_A \tag{3.8}$$

Here,

- S_{mass} is the mass source term. In the current case of spray drying, it is the mass addition per unit volume due to all the droplets inside a control volume,
- F_p is the sum of all relevant fluid-dynamic forces acting on all the particles in the averaging volume (V_{avg}),
- S_{mom} is another momentum source term and in the case of spray drying, it is the momentum flux due to mass transfer from the droplet surface,
- S_{energy} is the energy source term and refers to the rate of heat transferred to the fluid per unit volume of fluid by various mechanisms. In spray drying, this source term is due to the heat exchanged between the fluid and the droplet/particle,
- S_A is the species source term and is given by the rate of mass change of component A per unit volume of the fluid. In the current case, this change arises due to the solvent evaporating from the droplets into the surrounding fluid in a control volume.

The ideal gas model has been considered to describe the relationship between temperature, pressure and density.

A closer look at Equation 3.6 tells that the only unknown term in it is the term containing the fluctuating velocity u_i' and u_j', i.e., the fourth term on the right hand side of the equation. This term is referred to as the *volume-averaged Reynolds stress* and is analogous to the *Reynolds stress* in single-phase flow. The *volume-averaged Reynolds stress* is dependent on the turbulence in the averaging volume as well as the velocity deviations owing to the flow around the particles [17]. As detailed later in subsection 3.2.1, the two phases are one-way coupled in terms of momentum and the effect of dispersed phase on the momentum of continuous phase is insignificant. Also, the size of turbulent eddies formed by the particles is usually much smaller than that of the energy-containing eddies in the continuous phase, and hence, turbulence generated from movement of particles can be neglected [20]. Among the different options to model turbulence, the k-ϵ models based on the eddy viscosity concept (Boussinesq approximation) are considered to be a workhorse in practical engineering applications. Here, k is the turbulent kinetic energy and ϵ is turbulent dissipation. Despite there being limitations of the k-ϵ model for modeling turbulence in spray dryers, this model is preferred as it represents an acceptable compromise between accuracy and computational effort [1,19]. In this thesis, one of the variants of the k-ϵ model called the Realizable k-ϵ model is used as it better addresses the deficiencies of the traditional k-ϵ models [20]. That is, the realizable model features a certain constraint on the predicted stress tensor which ensures that the normal stresses are always positive, unlike the standard model in which the normal stresses can become negative for flows with large mean strain rates. In order to avoid having dense mesh very close to the walls or due to the reason that particular turbulence models are not valid very close to the walls, the use of semi-empirical rules called wall functions is needed. In this thesis, implementation of scalable wall functions for near-wall treatment produces consistent results for grids of arbitrary refinement. In ANSYS Fluent, the law-of-the-wall are based on the non-dimensional wall unit, y*, rather than y+. Scalable wall functions avoid the deterioration of standard wall functions under grid refinement below y*<11. [21].

The dispersed phase is modeled in the Lagrangian framework and is tracked using the Newton's second law of motion, and for a single droplet/particle is given by:

$$F_p = m_p \frac{dv_i}{dt} = 3\pi\mu_c d_p(u_i - v_i) + V_p\left(-\frac{\partial p}{\partial x_i} + \frac{\partial \tau_{ik}}{\partial x_k}\right) + \frac{\rho_c V_p}{2}\frac{d}{dt}(u_i - v_i) + \frac{3}{2}d_p^2\sqrt{\pi\rho_c\mu_c}\left[\int_0^{\tau_p}\frac{1}{\sqrt{t-t'}}\frac{d}{dt'}(u_i - v_i)dt' + \frac{(u_i - v_i)_0}{\sqrt{t}}\right] + m_p g_i + \Sigma F_{other} \quad (3.9)$$

Equation 3.9 is based for spherical particles in an unbounded flow field and for Re_p<1. The terms in the order written on the right-hand side of Equation 3.9 are drag force, force due to pressure and shear stress fields in the flow undisturbed by the presence of the particle, added mass force, Basset force and force due to gravity, respectively. Here, ΣF_{other} includes any other forces acting on a droplet/particle due to the gas phase such as Saffman and Magnus lift forces, thermophoretic force, force due to Brownian motion, etc. ΣF_{other} also includes contact forces due to other particles and walls of the spray drying chamber.

The drag force is a resistance force which acts on the droplet/particle when there is no acceleration of relative velocity between the particle and the conveying fluid. To account for variation in particle Reynolds number, a drag coefficient, C_D is introduced in the term for drag force. The variation of drag coefficient with Reynolds number for a non-rotating sphere in uniform flow is shown in Figure 3.2.
In Fluent, the influence of particle Reynolds number on the drag co-efficient is taken into account through:

$$C_D = a_1 + \frac{a_2}{Re_p} + \frac{a_3}{Re_p^2} \quad (3.10)$$

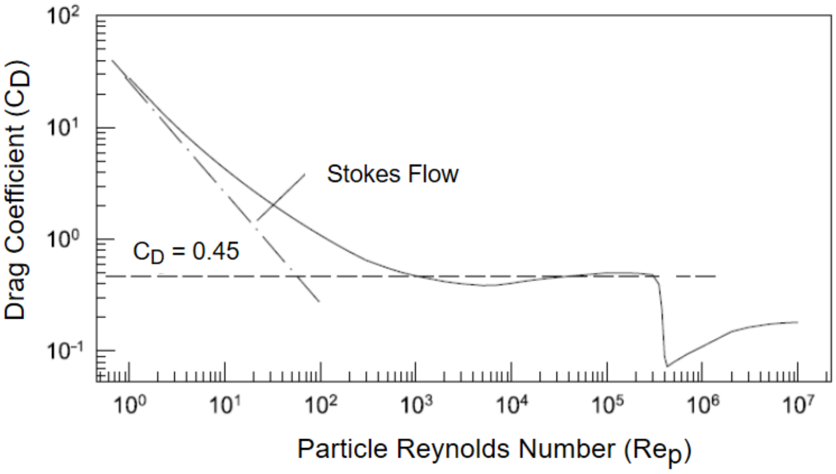

Figure 3.2: Variation of drag coefficient of a sphere with Reynolds number. [17]

where a_1, a_2 and a_3 are constants that vary with Reynolds number [16].

In general, the droplet/particle also experiences force due to pressure gradient and shear stress in the conveying fluid. This is indicated by the second term on the right hand side of Equation 3.9. The added mass or virtual mass force is due to the acceleration of the fluid around the droplet/particle when the droplet itself is accelerated. The Basset force accounts for the force due to temporal delay in boundary layer development as the relative velocity between the fluid and the particle changes with time.

For the current spray dryer system, force due to pressure gradient and shear stress in the conveying fluid, added mass force and Basset force have been neglected. This is because all these forces are a function of the ratio of fluid density to droplet/particle density, and for a gas-liquid/solid system, this ratio is of the order of 10^{-3}. Among other forces, thermophoretic forces can be neglected considering the absence of temperature gradient in the direction normal to the direction of movement of the dispersed phase. Since the current case does not deal with sub-micron particles, force due to Brownian motion too, can be neglected. The absence of collisons, which could lead to rotation of particles, and the absence of velocity gradient in direction normal to flow are reasons enough to neglect Magnus and Saffman's lift force, respectively. The presence of shear close to the atomizer also makes the particles rotate, however, these rotational forces are neglected. Due to negligible particle-particle interaction as detailed in subsection 3.2.2, the contact forces are also neglected. Thus, drag and gravity are the only significant forces acting on the dispersed phase.

3.2.1 Coupling between phases

Multiphase flows can be analysed through the concept of coupling. Phases can be coupled through exchange of momentum, mass and energy between them. Interaction between phases may be grouped into four phase-coupling categories. A system is said to be 'one-way coupled' if the continuous phase affects the dispersed phase but the dispersed phase does not affect the continuous phase. If the dispersed phase also affects the continuous phase, then the system is said to be 'two-way coupled'. If continuous phase affects the dispersed phase and vice-versa and disturbance of the fluid locally affects particle motion, then the system is said to be 'three-way coupled'. When in addition to the factors in three-way coupling, particle collisions are also significant, then the system is said to be 'four-way coupled'. [18]

The effect of two-way coupling can be taken into account through the inter-phase exchange terms. In other words, the effect of the dispersed phase on the continuous phase can be accounted for through the terms S_{mass}, F_p, S_{mom}, S_{energy} and S_A in Equation 3.5, Equation 3.6, Equation 3.7, Equation 3.8. For evaporating droplets, S_{mass} is given by:

$$S_{mass} = -\sum_k \dot{m}_{p,k}/V_{avg} \tag{3.11}$$

For spray-drying system, $\dot{m}_p$ can be obtained from Equation 3.1 for all the particles in the averaging volume which is the volume of a computational cell. Also, S_{mass} is equal to S_A since 'A'(i.e., solvent in the droplet) is the only species evaporating into the continuous phase and there is no other source for production of 'A' in the continuous phase (such as chemical reaction).

One way to understand if coupling is significant is by estimating a coupling parameter for mass(Π_{mass}), momentum(Π_{mom}) and energy(Π_{energy}). In general, if $\Pi_{mass}, \Pi_{mom}, \Pi_{energy} \ll 1$, it can be concluded that coupling effects are unimportant. For the system under consideration, as detailed in the Appendix, the value for $\Pi_{mass} \gg 1$ and thus, indicates that the system needs to be implemented as 'two-way coupled' for mass coupling. It is worth noting that the rate of mass evaporated from the droplets is very small when compared to the mass flow rate of the continuous phase and hence, this source term can be quite insignificant in the continuity equation but important to include in the species equation for the continuous phase. This mass coupling is implemented in Fluent when two-way coupling is enabled and is implemented as:

$$S_{mass} = \frac{\Delta m_p}{m_{p,0}} \dot{M}_{p,0}/V_{avg} = S_A \tag{3.12}$$

The interphase exchange terms for momentum are terms F_p and S_{mom}. As mentioned earlier, S_{mom} is the momentum flux to the continuous phase due to mass transfer from the droplets and can be accounted as:

$$S_{mom} = -\sum_k v_{i,k} \dot{m}_{p,k}/V_{avg} \tag{3.13}$$

The forces acting on the particle has an equivalent effect on the fluid phase. Hence, this effect is same in magnitude but with an opposite sign as that given by Equation 3.9, and since drag and gravity are the only significant forces, F_p is given by:

$$F_p = \frac{\pi d_p^2}{8}\rho_c C_D \mid u_i - v_i \mid (u_i - v_i) + m_p g_i \tag{3.14}$$

In Fluent, this is implemented as:

$$F_p = \sum_s^n \Big((\frac{18\mu_c C_D Re_p}{\rho_p d_p^2 24}(v_i - u_i) + g_i)\dot{M}_p \Delta t_s \Big) \tag{3.15}$$

The degree of momentum coupling between the phases can be analysed with the help of momentum coupling parameter (Π_{mom}) given by:

$$\Pi_{mom} = \frac{Z}{1 + St_{mom}} \tag{3.16}$$

$$St_{mom} = \frac{\tau_v}{\tau_f} \tag{3.17}$$

where the particle relaxation time (τ_v) in Stokes regime is given by:

$$\tau_v = \frac{\rho_p d_p^2}{18\mu_c} \tag{3.18}$$

For the current case, as detailed in the Appendix, Π_{mom}«1 indicates that the system could be solved as 'one-way coupled' with respect to momentum. This means that F_p in Equation 3.6 could be neglected but is important in the case of droplet/particle in Equation 3.9. Also, S_{mom} can be neglected due to that the momentum from the small amount of evaporated mass is much less when compared to the momentum of the continuous phase. In Fluent, there does not exist an option to include this particular momentum source and there is not a way to decouple momentum separately while keeping the mass and energy coupling.

The source of energy in the continuous phase in spray drying is a result of heat exchange with the dispersed phase and is given by:

$$S_{energy} = -\frac{1}{V_{avg}} \sum_k q_k \tag{3.19}$$

For the spray drying system under consideration, q_k is equivalent to the first term on the right hand side of Equation 3.3 for every particle in the computational cell.

In Fluent, the thermal energy coupling is implemented as:

$$S_{energy} = (\frac{\dot{M}_{p,0}}{m_{p,0}}\Big[(m_{p_{in}} - m_{p_{out}})[-h_{lat}] - m_{p_{out}} \int_{T_{ref}}^{T_{p_{out}}} c_{p,p} dT + m_{p_{in}} \int_{T_{ref}}^{T_{p_{in}}} c_{p,p} dT\Big])/V_{avg} \tag{3.20}$$

For the current case, as detailed in the Appendix, Π_{energy}»1 and thus, indicates that system is 'two-way coupled' in terms of energy. Overall, the spray dryer is modeled as a 'two-way coupled' system.

3.2.2 Particle-particle interaction

In addition to the dispersed phase getting affected by the continuous phase, droplets/particles can also be affected by other droplets/particles. Hence, it is important to understand if particle-particle interactions are significant in the system of interest. In this regard, flows can be characterised as dilute and dense.

Dilute dispersed flow is one in which the particle motion is controlled by the fluid forces. On the other hand, in dense flows, particle motion is controlled by collisions or continuous contact.

Quantitatively, volume fraction of the dispersed phase (α_d) provides a general indicator for dilute or dense flows. It is defined as:

$$\alpha_d = \lim_{\delta V \to \delta V_o} \left(\frac{\delta V_d}{\delta V} \right) \tag{3.21}$$

where δV_o is the size of the averaging volume in which the variations of the averaged property become insignificant. In essence, this averaging volume must be greater than the particle volume but lesser than the physical dimensions of the system. As a rule of thumb, for dispersed phase volume fraction of 0.001 or smaller, the flow can be regarded as dilute [17].

An extreme case for the volume fraction can be considered to occur at the cell adjacent to the injection point, where the droplets have not dispersed yet. As detailed in the section A.2 in Appendix A, the calculated volume fraction for this extreme case is 0.006. However, looking at the volume fraction contour plot, i.e., Figure A.1 in section A.2, it is clear that the region in which the volume fraction is higher than 0.001 is very close to the injection point and constitutes a negligible volume when compared to the entire spray dryer volume. As can be seen from the contour plot, the volume fraction is much less than the threshold value of 0.001, and thus, allows to consider the flow to be dilute.

Apart from collisions, it is important to understand if agglomeration has to be considered. For the current system, laser measurements at different levels close to the spray show no indication of increase in particle size. Additionally, analysis of particle morphology shows no sign of agglomeration. Thus, it can be concluded that agglomeration is not significant in the spray dryer under consideration.

3.3 Particle tracking

The broader concept of Lagrangian particle tracking can be classified into two different methods namely the Discrete Element Method (DEM) and Discrete Parcel Method (DPM), as schematised in Figure 3.3. The Discrete Element Method is particularly applicable to contact-dominated flows. The Discrete Parcel Method involves identifying a group of particles, also known as parcel, and tracking the parcel through the flow field. Parcel is a group of representative particles having the same properties like size, velocity and temperature. This concept of tracking parcels instead of particles is appreciated in systems with large number of particles where tracking each and every particle may not be computationally feasible. The DPM is further divided into two classes depending on whether the flow in the system is non-dense or dense. A non-dense flow is one in which the fluid dynamic forces play the major role on particle motion but also includes cases where particle-particle collisions can be a contributing factor. On the other hand, in dense flows, particle motion is dominated by particle-particle interaction. [17]

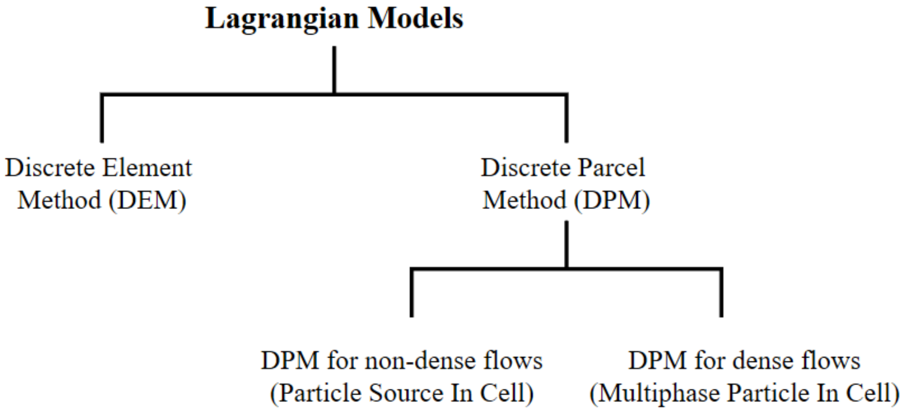

Figure 3.3: Schematic showing the branching of Lagrangian models.

In the current case, as seen earlier, particle-particle interaction is not significant and the particle motion is majorly influenced by the fluid dynamic forces and thus, the dispersed phase is tracked using the DPM approach for non-dense flows.

In the DPM approach, parcels of dispersed phase are tracked at every time step taking into account the influence of transient nature of continuous phase on the parcel [17]. This can be implemented through 'Unsteady Tracking' method in Fluent. Here, each particle is advanced by a specified number of time steps before the continuous phase flow solution is updated. 'Unsteady Tracking' can also be used when particle-particle interactions are significant in a system, however, this requires enabling a separate sub-model to account for collisions. [21]

A precursor to the DPM is the 'trajectory method' in which particle trajectories are used to quantify the properties of the dispersed phase [17]. In this method, the trajectories are calculated by advancing the particles through the domain according to Equation 3.9, until it reaches its final destination. As the particles travel through the trajectories interacting with the flow, they also contribute to the source term in each of the computational cell in their path. These source terms influence the continuous phase solution, which in turn affects the dispersed phase and thus, a new set of particle trajectories is calculated. This sequence is repeated until convergence is reached resulting in no change in the continuous phase fields and the dispersed phase trajectories. The advantage of this method is appreciated in its ease of implementation in systems where continuous phase is solved for as steady state.

In the current case, since the continuous phase is treated as steady state (detailed in subsection 4.2.2), the dispersed phase is tracked using the ’trajectory method’. In Fluent, this ’trajectory method’ is implemented using the ’Steady Tracking’ option.

Solving for the particle trajectory and other variables such as mass and temperature requires that the solution of the continuous phase field properties is available. Particles are, then, advanced in time with particle velocity and fluid velocity at the corresponding particle position as inputs in Equation 3.9, thus, resulting in the construction of particle trajectory. Particle mass and temperature are calculated with input from fluid temperature and species concentration, again, at corresponding particle position. In cases where the phases are two-way coupled, the effect of the dispersed phase on the continuous phase is accounted in the form of source terms or interphase exchange terms in the balance equations, i.e., the terms S_{mass}, F_p, S_{mom} S_{energy}, S_A in Equation 3.5, Equation 3.6, Equation 3.7, Equation 3.8.

3.4 Turbulent dispersion

The solution of the volume-averaged Navier-Stokes equations for the continuous phase using turbulence models for the closure of turbulence terms results in mean velocity field. Since the turbulence in the continuous phase is not transferred to the dispersed phase through the mean flow fields, the effect of turbulence on the dispersed phase has to be accounted for separately. This can be achieved through a stochastic tracking model.

In the stochastic tracking approach, prediction of turbulent dispersion of particles is done by integrating the trajectory equations for individual particles, using the instantaneous fluid velocity, along the particle path during the integration. The instantaneous velocity is given by:

$$u = \langle u \rangle + u' \tag{3.22}$$

The trajectory is computed for a sufficient number of representative particles to include the random effects of turbulence on particle dispersion.

In this thesis, a variant of the stochastic model called the Discrete Random Walk (DRW) model is used. In the DRW model, the fluctuating velocity components are discrete piece-wise constant functions of time.

3.4.1 Discrete Random Walk Model

In the DRW model, the interaction of a particle with a succession of discrete stylized fluid phase turbulent eddies is simulated. Here, each eddy is characterised by a Gaussian distributed random velocity (u’, v’, w’) fluctuation and a time scale

(τ_e). [17]

In Fluent, the values of u, v and w that prevail during the lifetime of the turbulent eddy are sampled by assuming that they obey a Gaussian probability distribution as follows [21]:

$$u' = \zeta\sqrt{\overline{u'^2}} \tag{3.23}$$

where ζ is a normally distributed random number, and the remainder of the right-hand side is the local RMS value of the velocity fluctuations. For the k-ϵ model and its variants, the values of the RMS fluctuating velocity components can be obtained from the kinetic energy of turbulence as follows:

$$\sqrt{\overline{u'^2}} = \sqrt{\overline{v'^2}} = \sqrt{\overline{w'^2}} = \sqrt{2k/3} \tag{3.24}$$

Turbulent dispersion is modeled by defining the characteristic lifetime of the eddy as constant:

$$\tau_e = 2T_L \tag{3.25}$$

where T_L is the integral time and for k-ϵ model and its variants, it is given by:

$$T_L = 0.15\frac{k}{\epsilon} \tag{3.26}$$

3.5 Numerical considerations

A brief description of the various numerical methods employed in the model development is detailed below.

3.5.1 Pressure-based flow solver

In the pressure-based approach, the velocity field is obtained from the momentum equations and the pressure field is extracted by solving a pressure or pressure correction equation which is obtained by manipulating continuity and momentum equations. This leads to the governing equations becoming non-linear and coupled to one another and hence, the solution process involves iterations where the set of governing equations are solved repeatedly until the solution converges. This can be done by either a segregated or a coupled algorithm. The coupled algorithm is detailed below.

3.5.2 Coupled algorithm

As the name suggests, this algorithm solves the system of governing equations simultaneously, as opposed to solving them sequentially in the segregated algorithm. Since the equations are solved in a closely coupled manner, the rate of solution convergence significantly improves when compared to the segregated algorithm. However, the memory requirement is higher than that of segregated algorithm. This is due to that the discrete system of governing equations must be stored in the memory when solving for the velocity and pressure fields. As memory is not limiting, the coupled pressure-based solver is used in the current model.

3.5.3 Spatial discretisation schemes

Mostly, the discrete values of the variables solved for in the system of governing equations are stored at the centres of computational cells. However, to solve for the equations, the values at the faces of the cells are required and hence, must be interpolated from the cell center values. The algorithm to calculate these face values is called the discretisation scheme. When face values are estimated using linear interpolation of values from neighbouring cells, it is called central-differencing scheme. Schemes that let face values be dependent only on upstream conditions are called upwind schemes. Upwind schemes ensure physical reliability for convective flows, by taking into account the direction of flow.

In the first-order upwind scheme, the face value between two cells is equal to the value of the nearest upstream cell. However, when the flow is not aligned with the mesh, this scheme increases numerical discretisation error known as numerical diffusion.

The second-order upwind scheme estimates face values using information from two upwind cells. Higher-order schemes can be numerically unstable. However, it is a preferred choice since it has improved accuracy.

Finally, the convective terms are discretised using the second order upwind scheme and the diffusion terms using the second order central differencing scheme.

4

Methodology

In this chapter, the simulation set-up, and the choice of different modeling parameters based on sensitivity analysis will be described in detail.

4.1 Simulation setup

Setting up a CFD simulation begins with defining the geometry. The geometry which, in this case, represents the fluid path is then discretised into a number of small sub-volumes called computational cells. This step is known as grid generation or meshing. Then, the choice of different models define the system of equations that are to be solved to obtain the solution. It is worth mentioning that this system of partial differential equations are transformed to algebraic form before they are solved numerically in the discretised domain. Finally, the procedure is incomplete without the specification of appropriate boundary conditions and the parameters of the chosen models for the domain of interest.

4.1.1 Drying gas chamber

As mentioned in the case description, the drying gas chamber is modeled separately and the results from this analysis are used to define boundary conditions for the dryer. This reduces the computational load of the final dryer model. Modeling of this unit is important because of the non-axisymmetric position of the drying gas inlet pipe and to assess if there is any non-uniform distribution of mass flow rate across the fourteen different outlet tubes. The drying gas chamber with major dimensions is shown in Figure 4.1

The geometry is meshed with polyhedral cells with inflation layers at the wall and is shown in Figure 4.2. In order to capture the velocity gradients in wall normal direction correctly, we need to ensure wall y* values are within a certain range. Inflation layers help in achieving this and in this case, maintain a y*>11 in most of the wall regions. The orthogonal quality of the mesh is kept to be higher than 0.1 and the average aspect ratio is kept below 5, as per best practice guidelines for meshing [20]. A mesh sensitivity analysis with three mesh refinements is done to achieve grid independent results and is shown later in section 5.1. The model is developed with nitrogen as the fluid. In Fluent, the inlet boundary condition is given as ’mass flow inlet’ with an inlet mass flow rate of 40 kg/hr and the outlet boundary condition is given as ’pressure outlet’ with a gauge pressure of 0 Pa. The velocity boundary condition at the wall is the 'no-slip' condition. The realizable k-ϵ turbulence model which represents a balance between accuracy and computational effort is chosen and scalable wall functions are enabled.

The simulation is run in steady state using the pressure-based solver. The convective terms are discretized using the second order upwind scheme and the diffusion terms using the second order central differencing scheme.

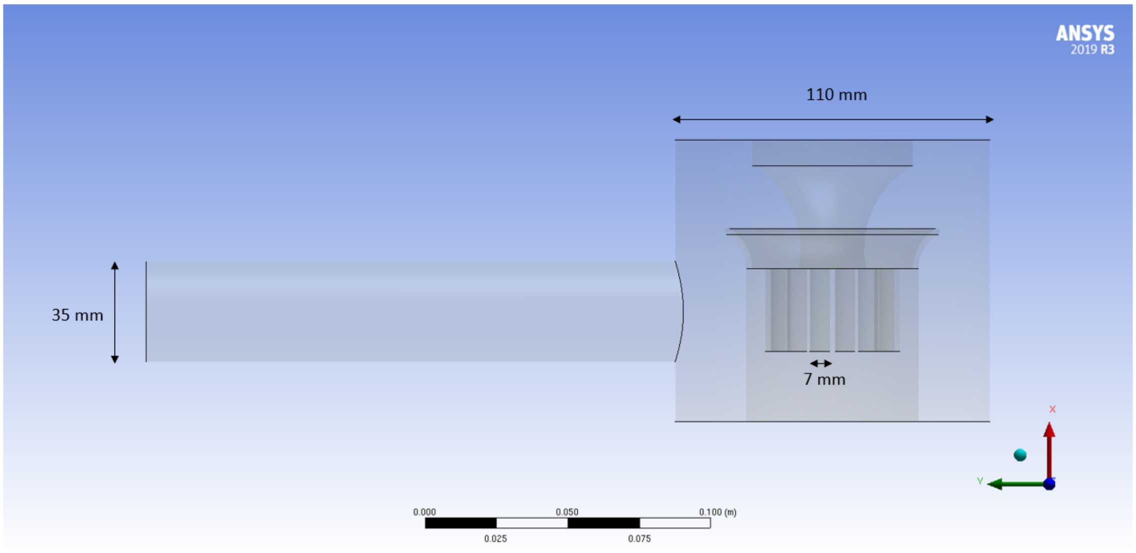

Figure 4.1: CAD model (from ANSYS) of drying gas chamber with major dimensions

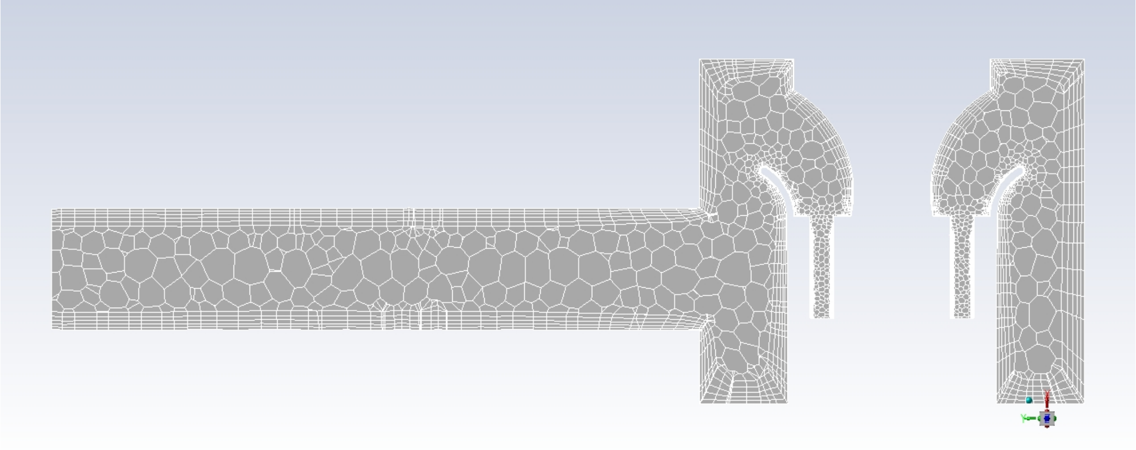

Figure 4.2: Polyhedral mesh (from ANSYS) of the drying gas chamber shown on a sectional plane

4.1.2 Atomizer

The atomizer model involves modeling of only the atomizing gas flow, and does not predict droplet formation. Modeling of the atomizing gas flow is important because it forms a significant amount, i.e., about 10-20% of the total gas flow rate in the dryer and it is this atomizing gas that is in contact with the injected solution close to the point of injection. The fields at the outlet of the atomizer can then be used as boundary conditions when tracking the droplet/particles in the dryer. The atomizer modeled in this thesis has an air-cap bore diameter of 2 mm which, in other words, can be understood as the outer diameter of the exit annulus. The diameter of the liquid nozzle is 0.8 mm and is important only when introducing droplet/particles in the domain. A CAD model of the fluid domain of the atomizing gas is shown in Figure 4.3 and the physical dimensions are shown in Table 4.1

Inlet	Outer diameter	12 mm
	Inner diameter	8 mm
Outlet	Outer diameter	2 mm
	Inner diameter	1.2 mm
Total length (from inlet to exit)		105.5 mm

Table 4.1: Physical dimensions of atomizing gas domain

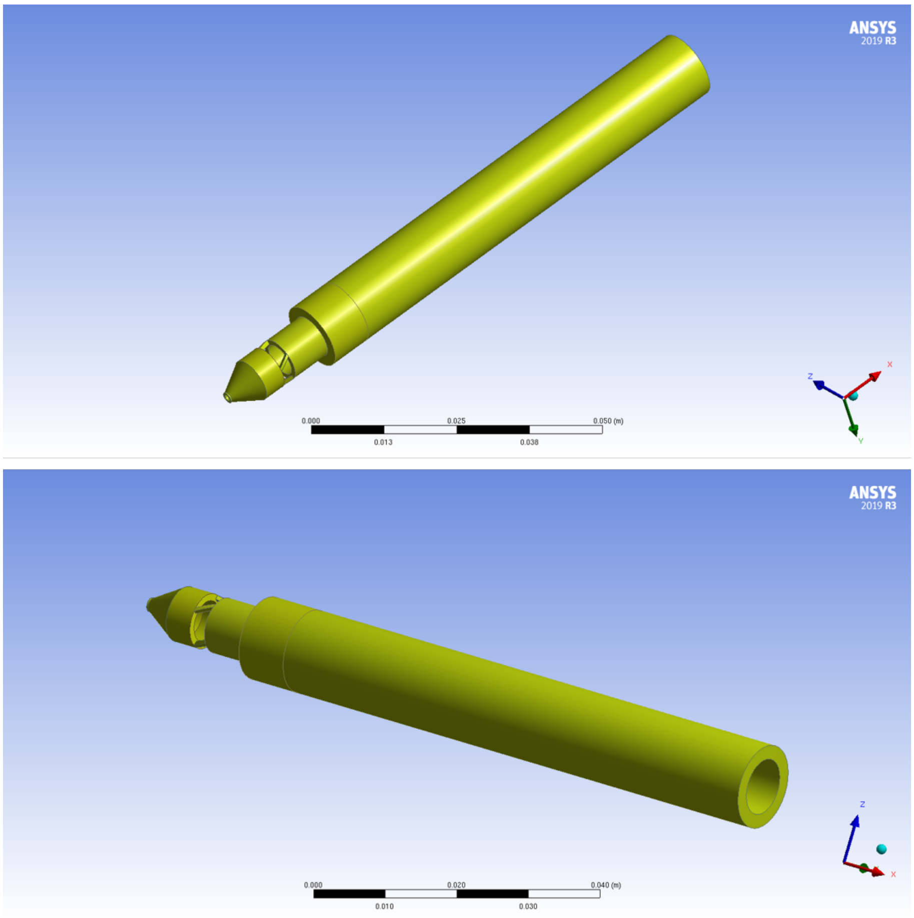

Figure 4.3: CAD model (from ANSYS) showing two different isometric views of atomizing gas fluid domain

To model the gas flow in the atomizer, the geometry of both the atomizer and the dryer are included. A comparatively coarser mesh is used in the dryer. The dryer is used in this model to avoid having a boundary condition at the outlet of atomizer. For an inlet flow rate of 2.7 Nm^3/hr, the characteristic velocity at the exit of the atomizer is in the range of 400 m/s resulting in a Mach number of 1.2. When the Mach number is greater than 1, the flow is said to be supersonic thus indicating that the flow through the atomizer is compressible. In Fluent, the pressure based solver has been, traditionally, used for incompressible flows but in newer releases it can handle a broad range of flows. Hence, the pressure-based coupled solver is used to model the gas flow in the atomizer.

The geometry is meshed with tetrahedral cells with inflation layers at the walls as shown in Figure 4.4. The minimum orthogonal quality of the mesh is kept to be 0.1 and the average aspect ratio is kept below 5, which is in accordance with the best practice guidelines for meshing [20]. A mesh sensitivity analysis with five mesh refinements is done to achieve grid independent results and a final mesh is chosen considering a balance between computational load and accuracy. The mesh sensitivity analysis is shown in section 5.2. The inlet boundary condition is given as 'pressure inlet' with a value of 2.6 barg and the boundary condition at the outlet of the dryer is given as 'pressure outlet' with a gauge pressure of 0 barg. The velocity boundary condition at the wall is the 'no-slip' condition. The various boundary conditions are summarised in Table 4.2. The realizable k-ϵ turbulence model which represents a balance between accuracy and computational effort is chosen and scalable wall functions are enabled. The energy equation is also solved since the flow is compressible and the density of the flow in the atomizer is dependent on pressure and temperature. The simulation is run in steady state. The convective terms are discretized using the second order upwind scheme owing to better accuracy and the diffusion terms using the second order central differencing scheme. Finally, the mass flow rate through the atomizer corresponding to the given inlet pressure is compared with experimental values from the manufacturer for the purpose of validation.

Boundary condition	**Unit**	**Value**
Inlet pressure for atomizing gas	barg	2.6
Inlet temperature for atomizing gas	K	298
Dryer outlet pressure	barg	0
Dryer outlet temperature	K	300

Table 4.2: Boundary conditions for atomizing gas in the atomizer

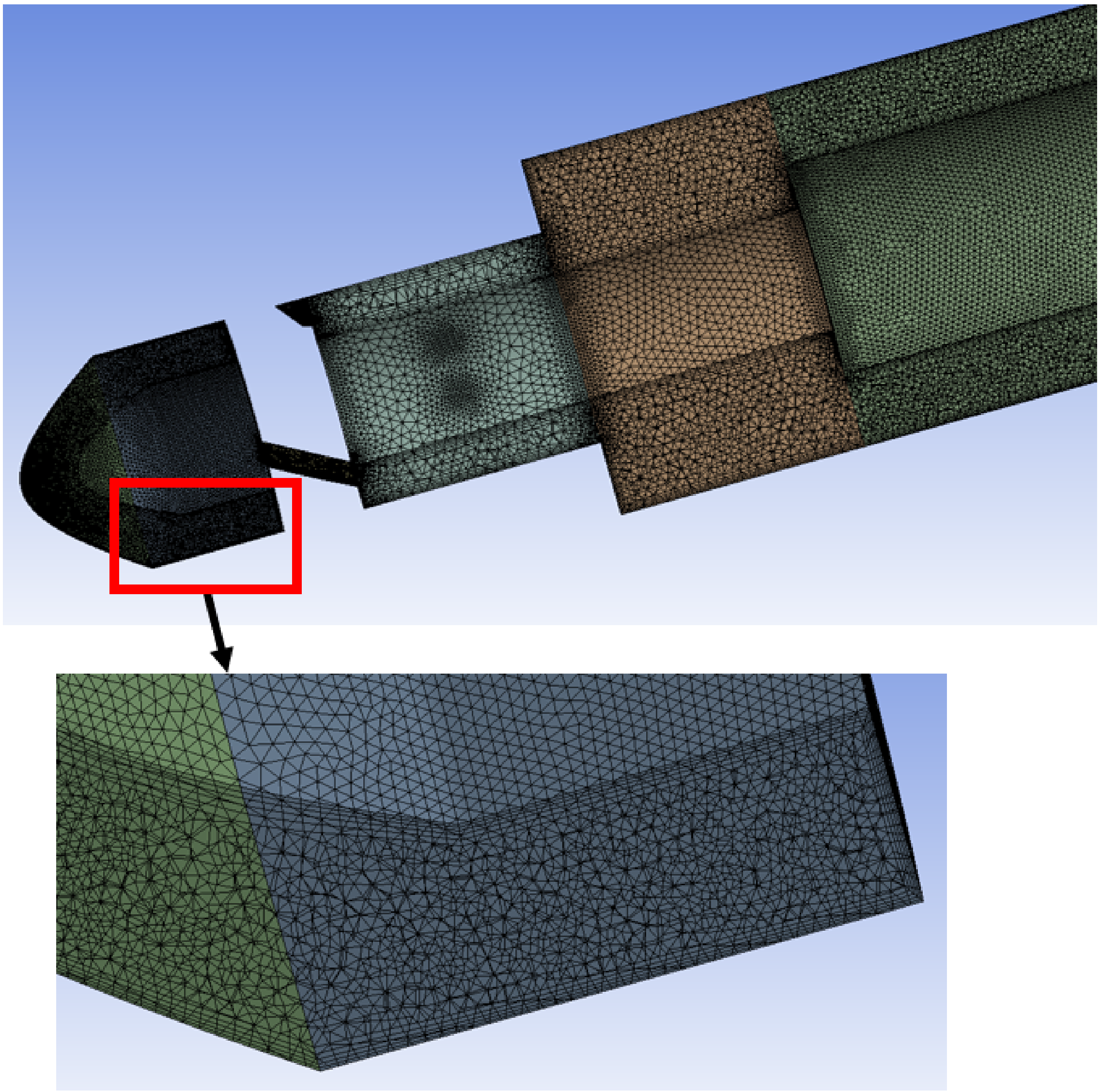

Figure 4.4: Sectional view (from ANSYS) showing the atomizer domain meshed with tetrahedral cells and inflation layers at the walls

4.1.3 Dryer

Once the atomizing gas flow is modeled, the drying gas is introduced in the dryer through the fourteen inlet tubes which have a diameter of 7 mm each. The simulation set-up for modeling the single phase flow and particle tracking is detailed below.

4.1.3.1 Single phase flow

The dryer is meshed with tetrahedral cells with inflation layers at certain walls as shown in Figure 4.5. Mesh independence is analysed with three mesh refinements and is detailed in subsection 5.3.1. The inlet boundary condition for the drying gas is given as 'mass flow inlet' with a value of 40 kg/hr (0.011kg/s). The inlet boundary condition for the atomizing gas is mapped with fields at the atomizer exit from the atomizer simulation. The outlet boundary condition is retained as 'pressure outlet' with a gauge pressure of 0 Pa. The velocity boundary condition at the wall is the 'no-slip' condition. The turbulence for the single phase flow in the dryer is modeled using realizable k-ϵ as it represents a good balance between accuracy and computational effort. The near-wall treatment is done with scalable wall functions. Scalable wall functions avoid the deterioration of standard wall functions under grid refinement below y*<11. Despite this, the inflation layers are introduced to keep the y*>11 to minimise error. It is worth mentioning that the y* of the walls in the conical region is already greater than 11 and hence, no inflation layer is introduced there. The pressure-based coupled solver is used as it can handle a broad range of flows. The convective terms are discretized using the second order upwind scheme owing to better accuracy and the diffusion terms using the second order central differencing scheme.

The simulation is first run in transient to understand if the flow in the dryer is inherently transient. However, it was realised that running in transient would be computationally expensive. Hence, the simulation was finally, run in steady state until convergence. The convergence of the steady state simulation was judged by monitoring the relevant parameters such as static pressure, static temperature and mass flow rate at the different boundaries of the system, such as atomiser outlet and dryer outlet, attained a steady value.

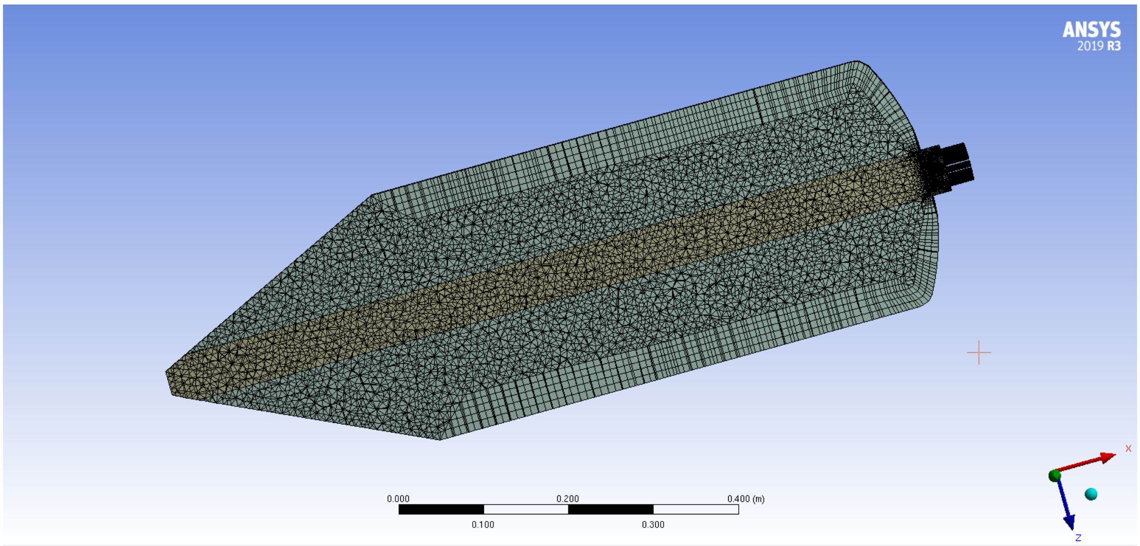

Figure 4.5: Sectional view (from ANSYS) showing the dryer domain meshed with tetrahedral cells and inflation layers at the walls

4.1.3.2 Particle tracking

Particle tracking is achieved by introducing the droplets in the dryer domain and by enabling the 'Discrete Phase Model' in Fluent. The 'Interaction with continuous phase' is enabled to take into account the exchange of heat, mass and momentum between the continuous and dispersed phase. The tracking parameters are specified in terms of two parameters:

- ’maximum number of steps’ - refers to the maximum number of time steps the droplets/particles are tracked for, before they are excluded from the calculation and reported as ’incomplete’ trajectories. The default value of 50,000 for maximum number of steps is retained and is chosen such that the number of recirculating particles that could lead to ’incomplete’ trajectories are kept within 15%. A comparatively lower percentage of incomplete particles leads to a corresponding increase in simulation time. Hence, this criteria of 15% incomplete particles is maintained until convergence in terms of constant exhaust temperature is reached, in order to have time effective simulation. However, when extracting the drying data, the maximum number of steps was kept such that there were negligible incomplete particles.
- ’step length factor’ - refers to the number of steps the particle takes to cross a computational cell. The default value of 5 is retained.

As detailed in section 3.2 in the Theory chapter, no other physical models other than the spherical drag model is enabled.

The droplets are introduced through ’Injections’ in Fluent. The particle type is chosen as ’Multicomponent’ through which it is possible to specify that the droplet contains a mixture of several components or species. These different components can, then, be attributed as vaporising or non-vaporising. The vaporising species is given to be water with a mass fraction of 0.95 and the non-vaporising species is given to be glucose with a mass fraction of 0.05. The point properties for the ’cone’ type injection is presented Table 4.3. As per the co-ordinate system under consideration, the position of the injection point represents the actual position of the liquid outlet of the atomizer. As the liquid solution flows down the dryer body, the injection is in the direction of negative x-axis. The cone angle has been set to zero to let the actual angle of the formed cone be as per the influence of flow of atomizing gas. The radius of the injection point is the same as the radius of liquid outlet of the atomizer. The mass flow rate is as received from lab data for which the corresponding velocity has been calculated considering the density of solution to be as that of water. The solution is injected at room temperature.

Parameter	**Unit**	**Value**
Position of injection point [X, Y, Z]	m	[0.942, 0, 0]
Direction of injection [X, Y, Z]	-	[-1, 0, 0]
Cone angle	deg	0
Radius of injection point	m	0.0004
Mass flow rate	kg/hr	0.42
Velocity magnitude	m/s	0.232
Temperature	K	298

Table 4.3: Point properties of the injection.

The droplet diameter is specified as a Rosin-Rammler distribution in which the mass fraction of droplets of diameter greater than d is given by:

$$Y_d = e^{-(d/\bar{d})^n} \tag{4.1}$$

where '$\overline{d}$' is the mean and 'n' is the spread parameter.

To obtain the parameters that define a Rosin-Rammler distribution, the data of droplet size distribution obtained from lab measurements is first expressed as 'Y_d' vs 'd' and plotted. This can be seen as the blue curve in Figure 4.6. The value for '$\overline{d}$' is obtained by noting the value of 'd' at which $Y_d = e^-1 \approx 0.368$. The numerical value of 'n' is obtained by estimating 'n(i)' for each of the different size ranges and taking an average. 'n(i)' is given by:

$$n(i) = \frac{ln(-ln\,Y_d)}{ln(d/\overline{d})} \tag{4.2}$$

Thus, the estimated paramaters are used to obtain a Rosin-Rammler curve fit and is plotted against the measured size distribution which is shown in Figure 4.6. The estimated parameters along with the minimum and maximum diameter of the size distribution are given as input to define the injection and the same is shown in Table 4.4.

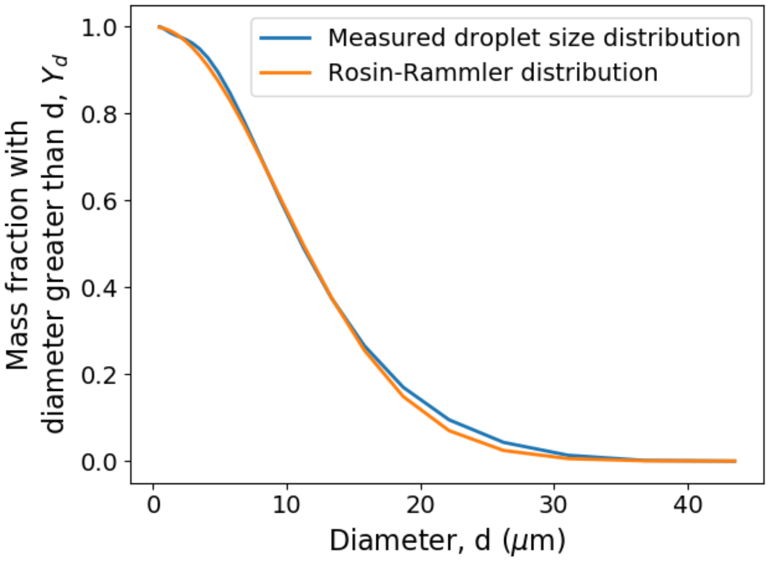

Figure 4.6: Plot showing Rosin-Rammler curve-fit against the measured droplet size distribution

Parameter	**Unit**	**Value**
Minimum diameter	μm	0.46
Maximum diameter	μm	43.5
Mean diameter, $\overline{d}$	μm	13.5
Spread parameter, n	-	1.97

Table 4.4: Parameters for Rosin-Rammler distribution

4.1.3.3 Other boundary conditions

The boundary conditions for the drying gas stream is summarised in Table 4.5. The combination of boundary conditions in Table 4.3 and Table 4.5 are for what will be called 'Case-1' simulations.

Boundary condition	Unit	Value
Inlet mass flow rate for drying gas	kg/hr	40
Inlet temperature for drying gas	K	385
Dryer outlet pressure	barg	0
Dryer outlet temperature	K	300

Table 4.5: Boundary conditions for drying gas

It is important to specify how the particles are treated when they reach a physical boundary. For this purpose, the boundary condition is set such that particles reflect when they hit the walls with both the normal and tangential reflection co-efficient set to 1 assuming a perfectly elastic collision with the wall. The particles are set to escape when they reach the outlet boundary.

Another important boundary is the walls of the dryer and the conditions for heat transfer present at these walls. The walls in the dryer are classified (Figure 4.7) based on the condition they present, i.e., whether it is insulated, allows for heat transfer, or is set at a certain temperature. 'Wall A' has no heat flux across it while there is heat loss across 'Wall B', and a constant temperature is maintained at 'Wall C'. The values for the corresponding boundary conditions, as estimated from a separate heat balance calculation, are given in Table 4.6. It is worth mentioning that the temperature for the heat tracing is set as equal to the temperature at the outlet of the spray dryer, as it is usually the setting for the equipment.

Name	Classification	Boundary condition
Wall A	Insulated	Heat flux = 0
Wall B	Heat transfer due to convection	Heat transfer co-efficient - 9.73 W/m2K Free stream temperature - 293 K
Wall C	Constant temperature	Temperature = 341.6 K

Table 4.6: Thermal boundary conditions at the walls of the dryer

The multiphase simulations are performed for another set of boundary conditions with changed values which will be called 'Case-2'. The changed boundary conditions along with the corresponding values are shown in Table 4.7. The remaining boundary conditions not mentioned below remain the same.

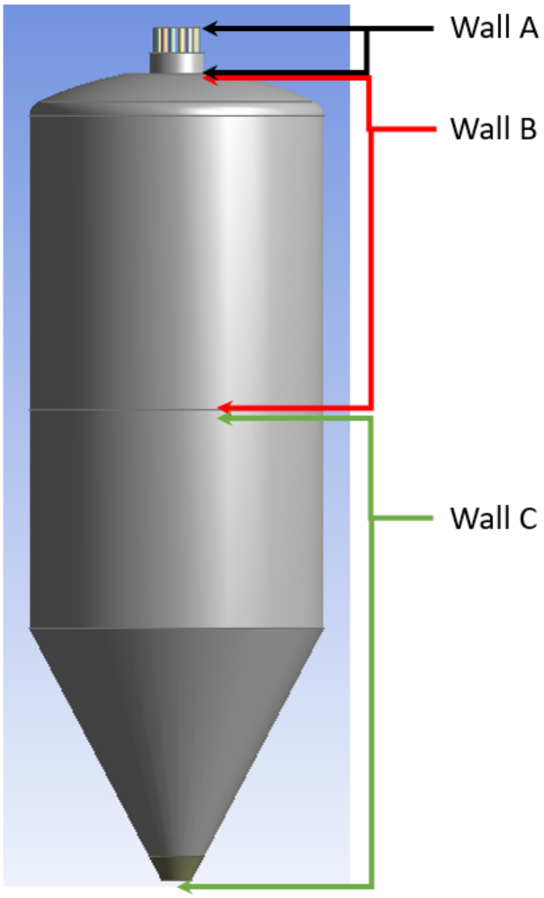

Figure 4.7: Classification of dryer walls based on boundary conditions.

Boundary condition	Unit	Value
Inlet temperature for drying gas	K	405
Mass flow rate of injection	kg/hr	0.75
Velocity magnitude of injection	m/s	0.414

Table 4.7: Changed boundary conditions for 'Case-2'.

4.2 Sensitivity Analysis

The choice of model parameters used in a numerical set up is considered accurate when the corresponding simulation results, in addition to having converged, can match with the experimental results. However, since the apparatus is in a good manufacturing practices(GMP) facility, it has not been feasible to make measurements of velocity and temperature profiles and residence time distribution. This has been due to heavy usage and also difficulty to modify this type of equipment. One way to overcome this limitation is to do a sensitivity analysis to decide on the choice of parameters and the same is presented below.

4.2.1 Turbulence dispersion and number of particles

In section 3.4, it was mentioned that to include the random effects of turbulence on particle dispersion, the trajectory is computed for a sufficient number of particles. In Fluent, this is done through 'Number of tries' when including the effect of turbulent dispersion. Additionally, to have a balance between computational load and accuracy, a suitable choice of total number of parcels in the domain has to be made. The total number of parcels that will be handled in the domain is a product of three parameters namely:

- Number of tries,
- Number of streams,
- Number of representative diameters (in the droplet size distribution).

Thus, a sensitivity analysis is done to finalise the choice of values for these parameters based on their effect on residence time of the particles. The residence time is obtained by introducing the particles in the flow field obtained from a steady state simulation. The flow field from steady state simulation is chosen because as illustrated in subsection 4.2.2, the final simulations are run in steady state, and hence, getting the residence time data in steady state will be a better representation. For the purpose of the analysis, four representative diameters are chosen and for each of these, the 'number of streams' and 'number of tries' is varied and the residence time distribution is obtained. The mean of the residence time is plotted for the different combinations and is shown in Figure 4.8.

As can be seen from Figure 4.8, irrespective of the 'number of streams', the mean residence time changes sharply when turbulent dispersion is included, i.e., when 'number of tries' is equal to or greater than 1. However, with further increase in the 'number of tries', the change in residence time is small, keeping well within 5% which is within the variability of the method. Thus, the value of 1 is chosen for 'number of tries' to include the statistically significant effect of turbulent dispersion on the droplets/particles.

The difference in residence time between varying 'number of streams' reduces with increase in 'number of tries'. This indicates that when sufficient number of particles (given as a product of 'number of tries', 'number of streams' and 'number of representative diameters') are in the domain, there is little difference in the residence time values. Therefore, 400 streams with 15 representative diameters are chosen to represent the injection, resulting in a total of 6000 parcels in the domain.

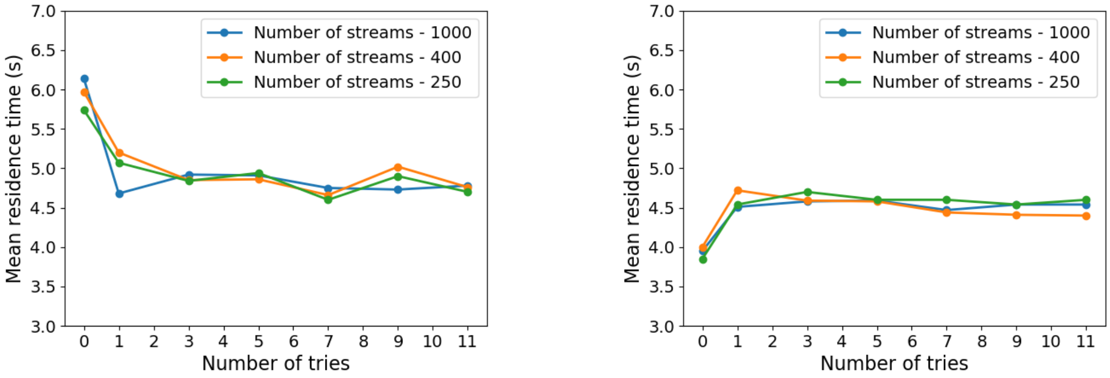

(a) Diameter 31.1 μm **(b)** Diameter 13.6 μm

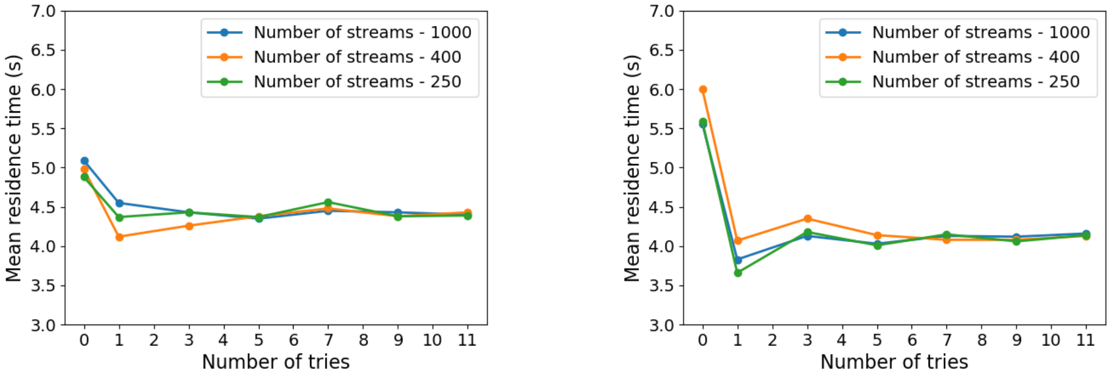

(c) Diameter 4.1 μm **(d)** Diameter 1.06 μm

Figure 4.8: Mean residence time of droplets for varying 'number of tries' and 'number of streams' for four representative initial diameters.

4.2.2 Steady vs Transient

Transient simulations for the continuous phase is run and the results from steady state simulation are used as initial condition. The results from the simulations of the continuous phase indicated that the flow in the dryer is not steady but is inherently transient in nature. The vertex-averaged velocity at several radial points along a diameter of the cross-section of the dryer, over a flow time of 0.01s is obtained and plotted. The changing velocity over time that can be seen in Figure 4.9 clearly indicates that the flow field in the spray dryer is transient. However, running transient simulation would mean increased computational load when compared with steady simulations even for single-phase flow. The transient simulation is run with first-order implicit time stepping and uses the adaptive time stepping algorithm in Fluent which is based on truncation error associated with the time integration scheme [21]. For a truncation error tolerance of 0.01 (recommended default value), a time step size of 1e-05s is maintained. The corresponding volume-averaged Courant number is less than 1, however, could have been higher considering the use of implicit scheme. The residence time of the flow in the spray dryer is calculated to be 4s. This would mean a total of 400,000 time steps. With the available computational resources, each time step requires 40s of wall clock time. This would result in 185 days of run time. Thus, a choice has to be made between running the simulations in steady or transient.

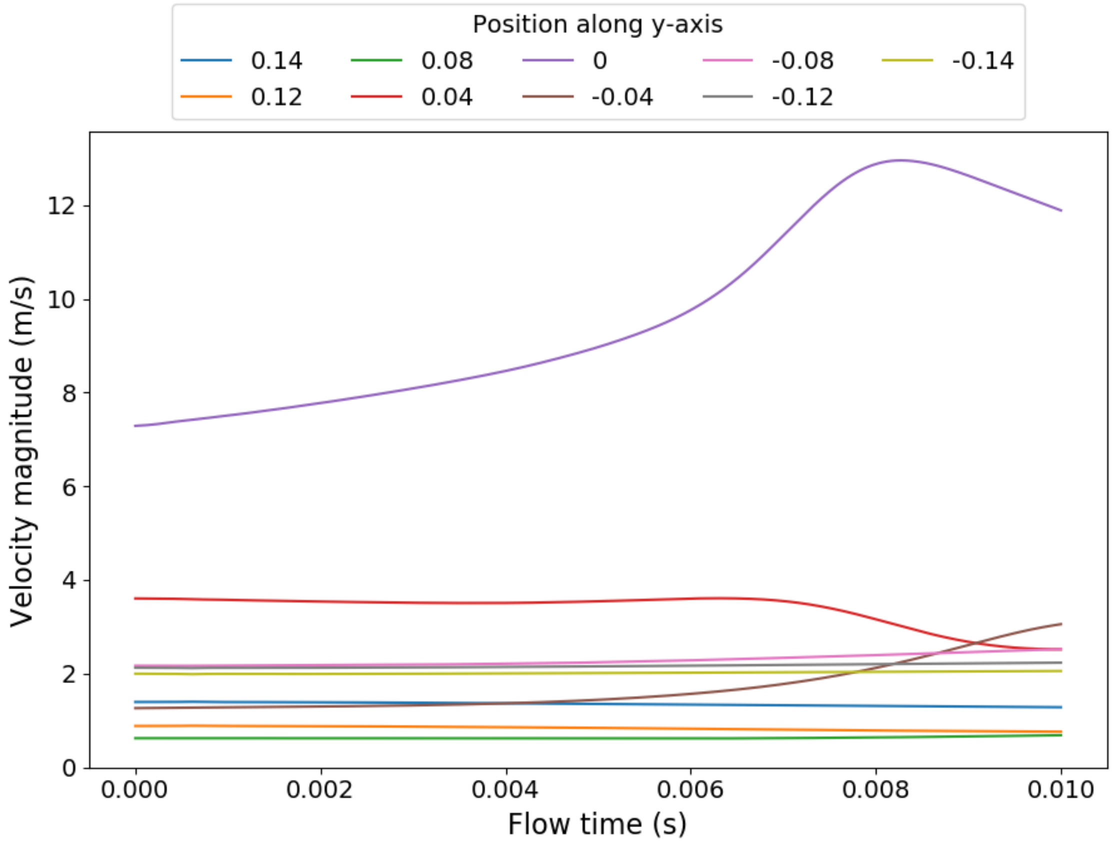

Figure 4.9: Vertex-averaged velocity at several points along y-axis of the dryer plotted over flow time.

To decide between steady and transient, the residence time of inert particles in the dryer domain is monitored to analyse if there are major differences between the two cases. The polydispersed droplets represented by Rosin-Rammler distribution (Table 4.4) are introduced in the steady and transient flow field and for the number of tries set to 1 (as detailed in subsection 4.2.1), the residence time distribution (RTD) on a mass basis sampled at the outlet of the dryer is obtained. For the steady simulation, the sampling is done at several iteration intervals. For the transient simulation run over a total flow time of 0.01s, sampling is done at five different intermediate flow times. For each sampling of all particle tracks, mean and standard deviation of the RTD are obtained. It is worth noting that this standard deviation is characteristic of how much back-mixing is present in the spray dryer, where a lower value is representative of plug-flow and a higher value is representative of a well-mixed system. The statistics of all the samples, in both the steady and transient case, such as average of mean RTD of all samples and the corresponding confidence interval, and the mean of dimensionless variance (DV) of all samples and the corresponding confidence interval are presented in Table 4.8. The dimensionless variance for each sample is calculated as ratio of square of standard deviation of RTD to square of mean of RTD of the respective sample. It can be seen that there is some difference between the mean residence times obtained for steady and transient simulations. The dimensionless variance is lesser in the case of transient simulation, indicating more consistent data for different samples. It is worth mentioning that the flow time within which the sampling for transient simulation is done is much smaller compared to flow time of single pass flow of the drying gas. However, this difference in mean RTD between steady and transient case is acknowledged and considering the high computational load, analysis of particle tracking and drying is performed with results from steady state simulations.

Case	**Statistics of mean RTD of all samples (s)**	**Statistics of DV of all samples**
Steady	4.4 ± 0.8	0.96 ± 0.06
Transient	3.5 ± 0.1	0.86 ± 0.07

Table 4.8: Statistics of RTD of different samples for steady and transient simulation.

5

Results

In this section, the results obtained from the single phase modeling of different geometries, and the droplet drying behaviour in the dryer is presented in detail.

5.1 Drying gas chamber

As mentioned in subsection 4.1.1, the drying gas chamber is modeled to analyse the distribution of mass flow across the fourteen different outlet tubes. Hence, the simulation results in the form of mass flow rate at the fourteen different outlets is analysed and plotted as a radar chart. Figure 5.1 shows the same for three mesh refinements where 1 to 14 represent the different outlets. The coarse, medium and fine refer to mesh with 348958, 561454 and 1557082 cells, respectively.

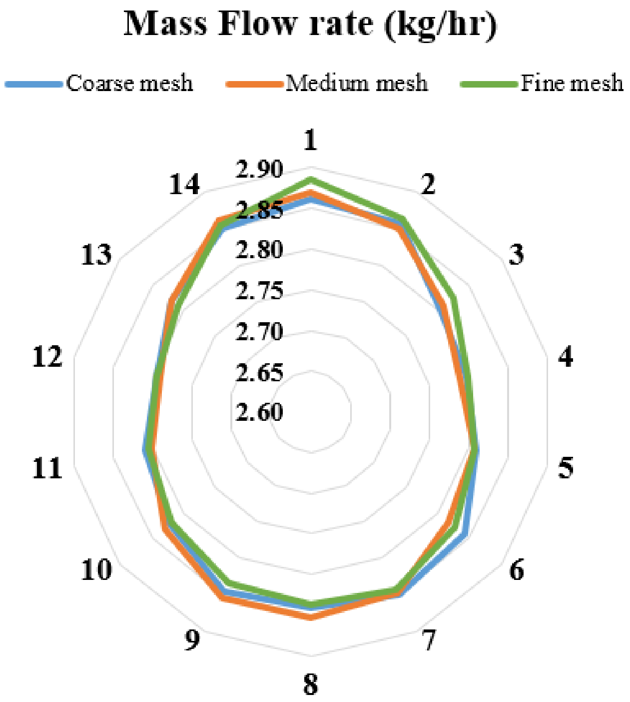

Figure 5.1: Radar plot showing mass flow rate (kg/hr) at the fourteen outlets for three mesh refinements of the drying gas chamber goemetry

As can be seen from Table 5.1, the relative standard deviation is around 1% and the variation among the flow rates at different outlets is around 3%. Such low

Parameters	Mass flow rate (kg/hr)		
	Coarse	**Medium**	**Fine**
Mean	2.829	2.829	2.829
Std. deviation	0.0235	0.0272	0.026
Relative std. deviation	1%	1%	1%
Variation among data	2%	3%	3%

Table 5.1: Summary of data

percentages are reasons enough to neglect the minor variations in the exit flow rates. The same can be inferred visually from the velocity contour plots as shown in Figure 5.2. Thus, in the dryer model, the total mass flow rate can be equally distributed across the fourteen inlets to the dryer. It is worth mentioning that the relative standard deviation is calculated as the ratio of standard deviation to mean, and the variation calculated as difference between the maximum and minimum value divided by the standard deviation.

(a) Sectional plane showing velocity contour

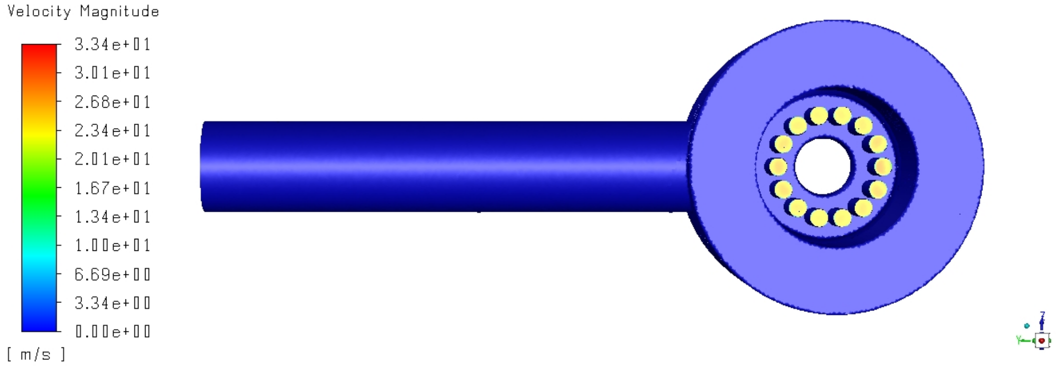

(b) Velocity contour on walls and the outlet.

Figure 5.2: Velocity contour plots (from ANSYS) of the drying gas chamber

5.2 Atomizer

The results from modeling of gas flow in the atomizer are presented here, and compared with the value in the product catalogue. As mentioned earlier in section 2.2, the atomizer with an air-cap position of ’5’ is used. The corresponding volumetric flow rate, as given in the product catalogue, for an inlet pressure of 2.6 barg is 2.7 Nm^3/hr at 20 ^{o}C. This translates to a mass flow rate of 3.1 kg/hr. For finalising the model, a mesh sensitivity study is performed to obtain grid independence. The different refinements are obtained by changing the base size of the cell and also varying a parameter called ’number of cells across gap’. This parameter affects the number of cells in a region which has close proximity. For an inlet pressure of 2.6 barg, the mass flow rate at the exit of the atomizer is monitored and is used as a parameter for obtaining grid independence. Figure 5.3 shows the variation of this parameter for the five mesh configurations and the mesh configuration (with 8.8 million cells), with a corresponding mass flow rate of 2.8 kg/hr, chosen for further analysis is highlighted. Comparing the catalogue value with the results from the model, a difference of approximately 10% has been observed for the current modeling approach.

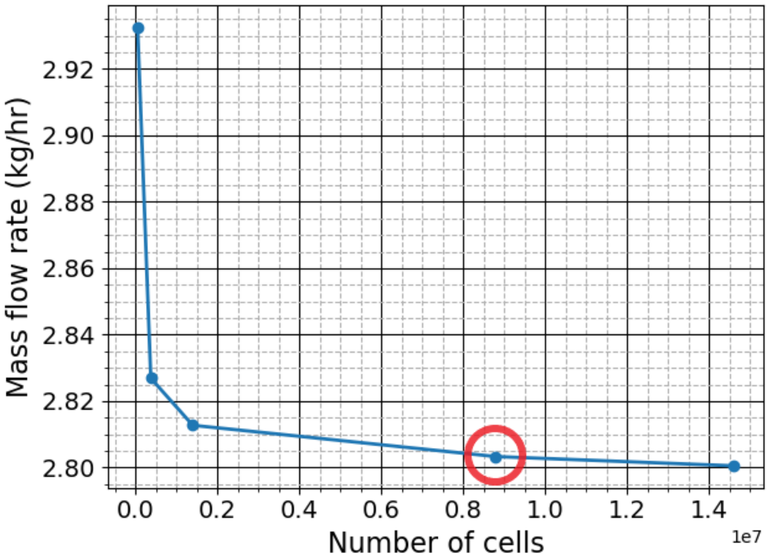

Figure 5.3: Atomizer mesh independence study based on mass flow rate at atomizer exit, for an inlet pressure of 2.6 barg. The mesh configuration chosen for further analysis is highlighted.

The contour plots for pressure, velocity and temperature are shown in Figure 5.4 (the contour is shown horizontally for presentation purpose, however, the atomizer and the spray dryer are positioned vertically in reality as detailed in chapter 2). Since it is shown on a sectional plane, the slits in the atomizer are visible as a gap in the figures. It can be seen from Figure 5.4a that the major pressure changes occurs at the transition through the slits and at the constriction present at the atomizer exit. Observing close to the exit of the atomizer, it can be seen that there is a decrease in pressure leading to expansion of the high pressure atomizing gas. This further leads to a decrease in local temperature which is consistent with what can be expected from isentropic expansion of an ideal gas. The velocity at the exit of the atomizer is greater than speed of sound, indicating supersonic flow as detailed in subsection 4.1.2.

(a) Pressure contour plot shown on a sectional plane of the atomizer

(b) Velocity contour plot shown on a sectional plane of the atomizer

(c) Static temperature contour plot shown on a sectional plane of the atomizer

Figure 5.4: Contour plots (from ANSYS) for pressure, velocity and static temperature in the atomizer, for the condition of inlet pressure of 2.6 barg.

5.3 Dryer

5.3.1 Mesh independence

Before the introduction of droplets/particles in the dryer, a mesh independence study is performed for the dryer domain. The different meshes are obtained by changing the base size of the cell. The parameter that is monitored for the purpose of mesh independence is the vertex-averaged velocity at several radial points along a diameter of the cross-section of the dryer and at different heights in the dryer, i.e., at about 0.4m, 0.6m and 0.8m from the outlet of the dryer. The results are plotted for three mesh configurations namely coarse, medium and fine with 294966, 588327 and 970295 computational cells respectively, as shown in Figure 5.5.

Additionally, inert particles were introduced in the dryer and the residence time distribution (RTD) at the outlet of the dryer was obtained for the three different mesh configurations. The sampling was done at five different flow times. The sampling was done in a transient simulation since the flow field is inherently transient as detailed in subsection 4.2.2. The polydispersed droplets represented by Rosin-Rammler distribution (Table 4.4) are introduced in the transient flow field and for the number of tries set to 1 (as detailed in subsection 4.2.1), the residence time distribution on a mass basis for all particle tracks at the outlet of the dryer is obtained. For each sample, mean and standard deviation are obtained. It is worth noting that this standard deviation is characteristic of how much back-mixing is present in the spray dryer, where a lower value is representative of plug-flow and a higher value is representative of a well-mixed system. For each of the samples obtained at different flow times, the dimensionless variance is calculated and the corresponding statistics, in terms of mean of all the samples and the corresponding confidence interval, are reported. The dimensionless variance is calculated as ratio of square of standard deviation to square of mean. The data for samples in a medium mesh is reported in Table 5.2. Similar data is obtained for coarse and medium mesh and the respective statistics of dimensionless variance is shown in Table 5.3.

As can be seen from Figure 5.5, the results from the medium mesh is closer than that from coarse mesh, to the results from the fine mesh. Also, as can be seen in Table 5.3, the dimensionless variance is least for the medium mesh indicating more consistent data for different samples when compared with other mesh configurations. Hence, the medium mesh is chosen for final analysis with particles.

The plot for residence time distribution of inert particles sampled on mass-basis, in medium mesh and from steady state flow field is shown in Figure 5.6. This is in line with the characteristic plot of an ideal Continuous Stirred Tank Reactor (CSTR). This agrees with the values of dimensionless variance close to one as shown in Table 5.2. Thus, the residence time distribution can be modeled as a CSTR with characteristic time equal to the obtained mean residence time.

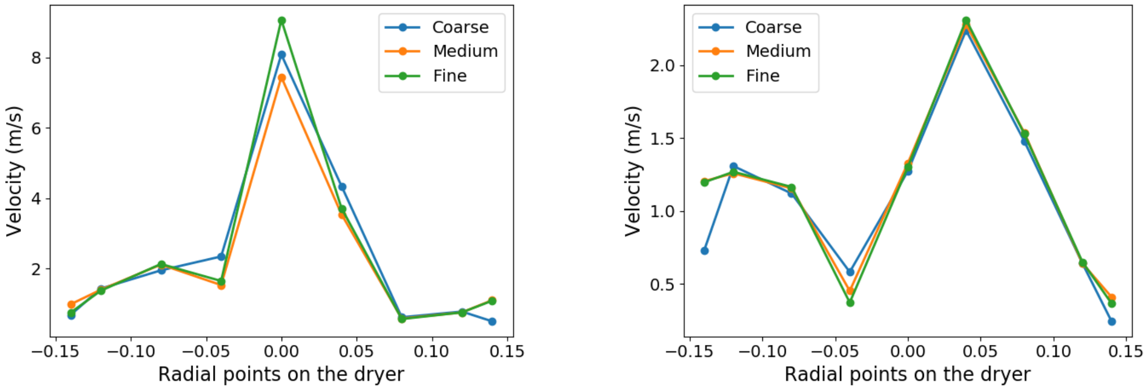

(a) At x = 0.8

(b) At x = 0.6

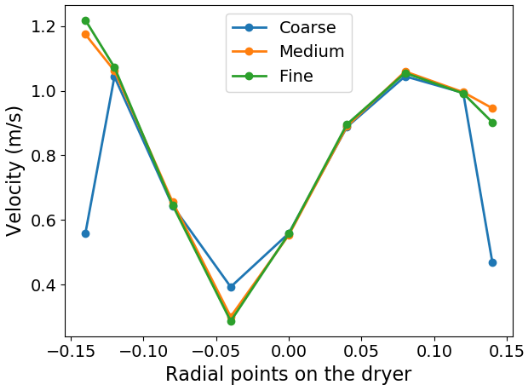

(c) At x = 0.4

Figure 5.5: Vertex-averaged velocity at nine different points at varying heights in the dryer for three mesh refinements plotted for the purpose of mesh independence study.

Sample	**Flow time (s)**	**RTD mean (s)**	**RTD Standard Deviation (s)**	**Dimensionless Variance**
1	0.001	3.6	3.4	0.89
2	0.003	3.5	3.1	0.78
3	0.006	3.5	3.2	0.84
4	0.008	3.3	3.2	0.94
5	0.01	3.4	3.1	0.83
Statistics of (dimensionless variance) all samples				0.86 ± 0.07

Table 5.2: RTD data taken for inert particles for number of tries set to 1 and at different flow times for the medium mesh.

Mesh configuration	Statistics of (dimensionless variance) of all samples
Coarse	0.96 ± 0.13
Medium	0.86 ± 0.07
Fine	0.91 ± 0.11

Table 5.3: Statistics of dimensionless variance for different mesh configurations.

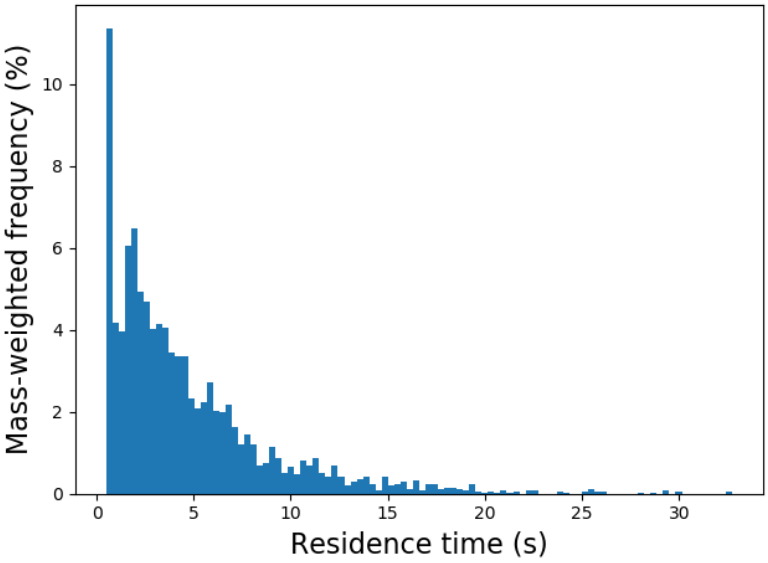

Figure 5.6: Mass-weighted residence time distribution of inert droplets introduced in the steady state flow field of the dryer.

5.3.2 Droplet drying

In this section, the results from the multiphase simulations after the introduction of the droplets and including the drying of the dispersed phase is presented and discussed. The drying of the dispersed phase simulated with the 'Case-1' boundary conditions described in subsubsection 4.1.3.3 is presented first. The contour plots for continuous phase velocity and static temperature on a sectional plane of the dryer is shown in Figure 5.7. Static temperature is defined as the temperature that would be shown by a measuring device that has no relative velocity to the fluid stream being measured. It can be seen from Figure 5.7a that the velocity is highest close to the atomizer exit, but that it is high, exists only for a short distance into the dryer. Further downstream, the velocity in the dryer is mainly due to the flow of the drying gas. The effect of isentropic expansion, as described earlier, is visible from the relatively lower temperatures close to the atomizer exit and can be seen in Figure 5.7b. Also, the temperature of the drying gas, which has a higher value at the inlet, decreases with flow through the dryer. This is owing to the transfer of heat to the discrete phase for drying.

The resulting drying data is analysed for four different initial diameters: 6.6 μm, 12.8 μm, 25.1 μm and 37.4 μm. For each initial diameter, the drying data along 400 paths is obtained and analysed. It has been observed that, for the same initial

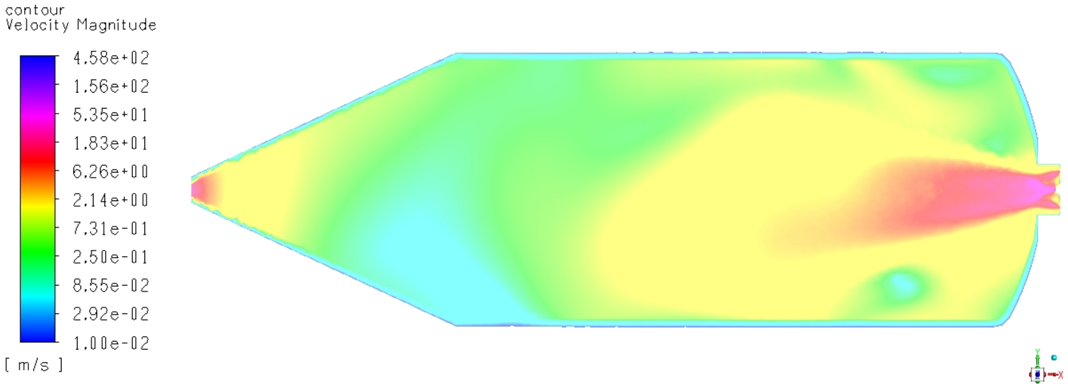

(a) Velocity contour plot shown on a sectional plane of the dryer.

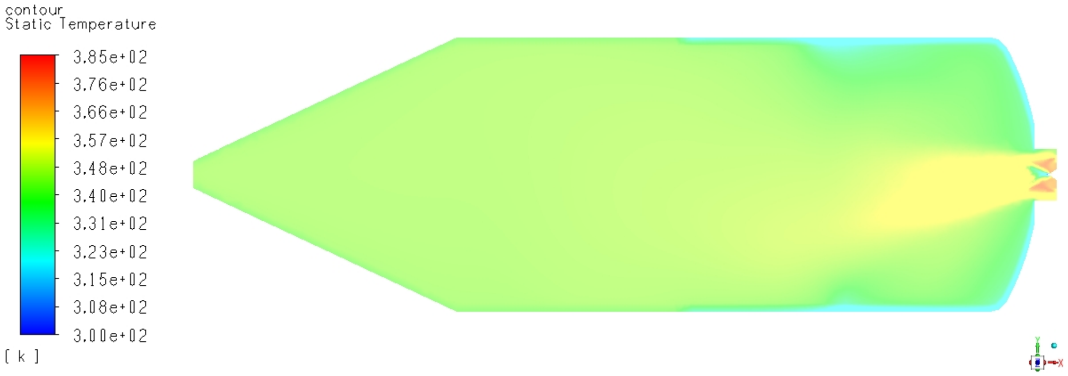

(b) Static temperature contour plot shown on a sectional plane of the dryer.

Figure 5.7: Contour plots (from ANSYS) for velocity and static temperature in the dryer, pertaining to 'Case-1' boundary conditions (as detailed in subsubsection 4.1.3.3).

diameter, the drying rate is different along the different trajectories of the dispersed phase, and hence, a drying rate distribution is obtained and is shown in Figure 5.8. The drying rate is estimated as rate of change of the square of the droplet diameter.

An important dimensionless parameter that has been identified to influence particle formation is the Peclet number which is the ratio of the evaporation rate (or drying rate) and the diffusion co-efficient of the solute [9]. For the analysis of the drying data, a diffusion co-efficient of 6 x 10^{-10} m^2/s has been used. This value is similar to diffusion co-efficient of components such as tyrosine and isoleucine in water [22,23]. The distribution of Peclet number for different initial diameter of the dispersed phase is shown in Figure 5.9.

It can be seen from Figure 5.8e that as the droplet diameter increases, the mean rate of drying decreases. A similar trend can be observed for the mean Peclet number as well, as shown in Figure 5.9e.

The solute concentration as a function of the droplet/particle radius is estimated in accordance with the equations in the paper by Vehring et. al. [9] and are detailed in the section A.3. The resulting data is plotted as shown in Figure 5.10 and Figure 5.11 for two different drying rates, high and low, and for droplets with different initial diameters. A profile of solute concentration appears in the droplet/particle due to the receding droplet surface which occurs as the solvent evaporates. In each of the plots, the concentration profile of the solute in the droplet as drying takes place is plotted. The bottom-most curve in the plot represents the concentration profile when drying is in its initial state, and is evident from the corresponding droplet diameter shown in the legend. In this initial state, the concentration profile is relatively flat and as drying progresses, the droplet diameter decreases and a profile of solute concentration evolves as can be seen from the upper-most curve in the plot.

As mentioned earlier, particle formation and hence, the particle morphology can be analysed through the Peclet number. For Pe ≤ 1, the diffusional velocity of the solute is faster or on the same order as the recession rate of the droplet surface. Thus, the radial concentration profile of the solute in the finally obtained particle is predicted to be flat. When small Peclet numbers are coupled with a large solute solubility, precipitation is expected to appear late in the evaporation process and relatively homogeneously throughout the droplet. The resulting dry particles are expected to have little or no void space. The experimental results by Vehring et. al. indicate the same where trehalose solution was dried. The initial Peclet number was less than 1 and the typical morphology of the dried particle was solid with minimal voids, indicating a flat radial concentration profile. [9]

As against low Peclet number, large Peclet numbers can cause an enrichment of the solute at the droplet/particle surface which likely leads to shell or skin formation, resulting in formation of hollow particles. This is due to the verified hypothesis that a large Peclet number indicates that the surface recession is fast when compared to the diffusional motion of the dissolved molecules. The results from experiments in which glycoprotein particles were dried, as reported in Vehring et. al. confirm the above hypothesis and the corresponding hollow particle morphology. That is, for high values of Peclet number, it was observed that the density of the glycoprotein particles was significantly lower than the corresponding pycnometer density. This indicates the presence of large void space in the particles. [9]

Analysis of the drying data obtained from the drying model developed in this thesis reveals similar trends. As the Peclet number for the droplet diameters under consideration is greater than 1, it can be observed from Figure 5.10 and Figure 5.11 that the initially equal radial distribution of the solute in the droplet changes gradually into a profile that shows strong surface enrichment, where the mass fraction at the surface eventually reaches a value of 1. Comparing the concentration profile plots for high and low drying rate, irrespective of the initial diameter, indicates that the gradient of solute mass fraction in the particle is higher in the case of high drying rate as compared with low drying rate. This can be attributed to the high and low values of Peclet number, respectively.

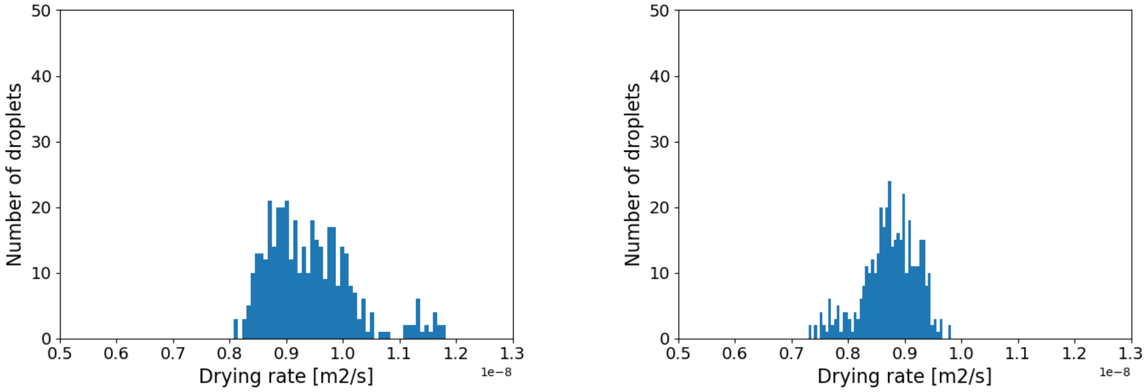

(a) For initial diameter = 6.6 μm

(b) For initial diameter = 12.8 μm

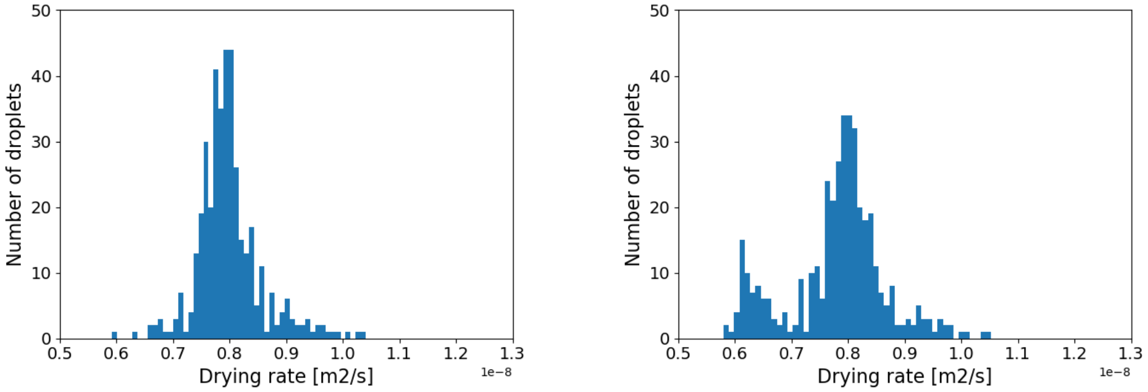

(c) For initial diameter = 25.1 μm

(d) For initial diameter = 37.4 μm

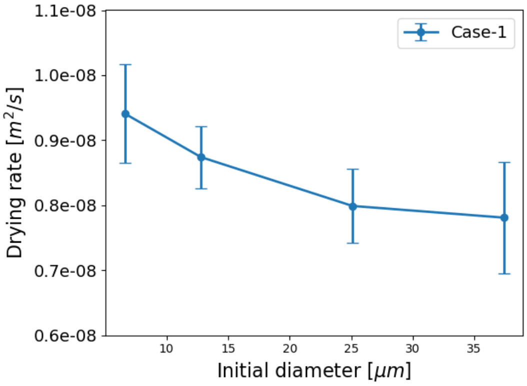

(e) Drying rate vs initial diameter

Figure 5.8: For 'Case-1' boundary conditions :- (a)-(d): Distribution of rate of drying for droplets of different initial diameter; for each initial diameter, the drying data along 400 paths is obtained and plotted. (e): Plot showing spread of drying rate for different initial diameter

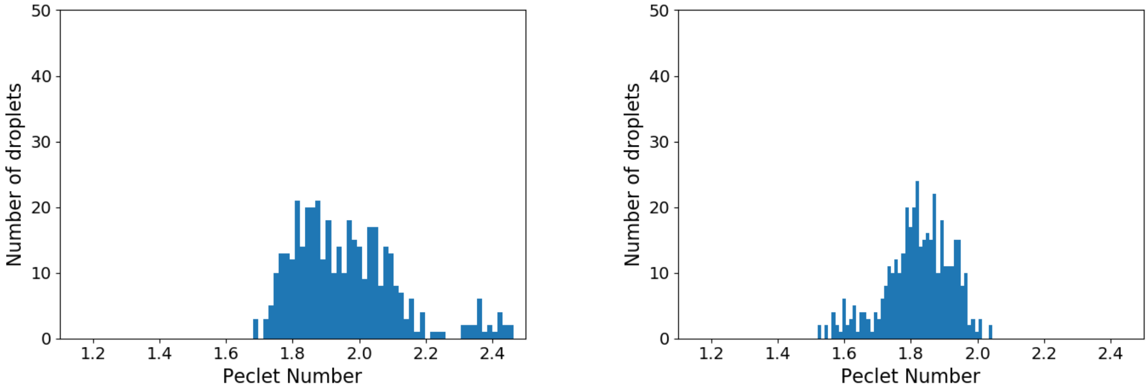

(a) For initial diameter = 6.6 μm

(b) For initial diameter = 12.8 μm

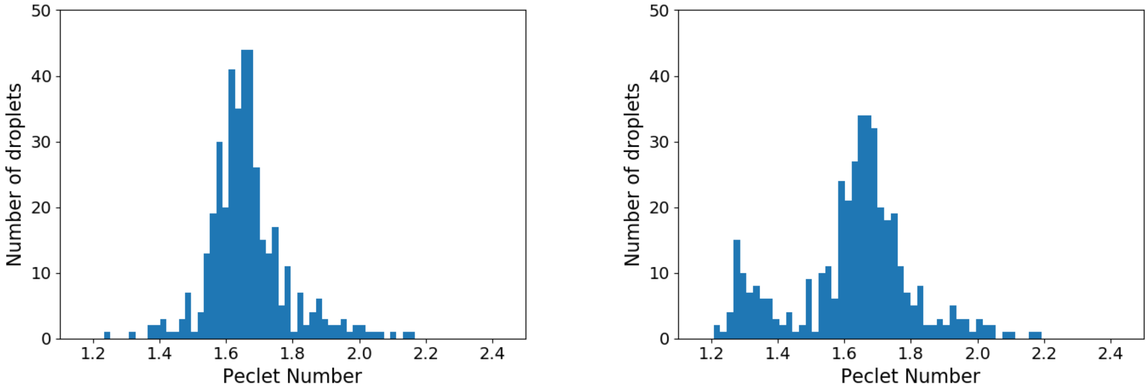

(c) For initial diameter = 25.1 μm

(d) For initial diameter = 37.4 μm

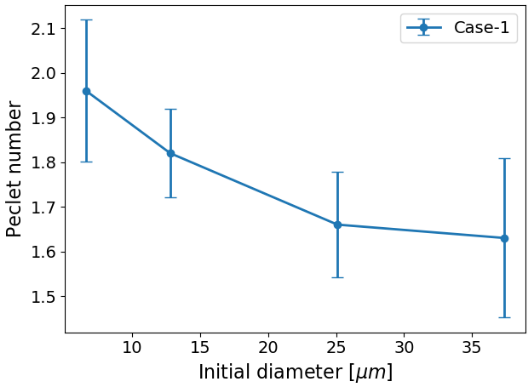

(e) Peclet number vs initial diameter

Figure 5.9: For 'Case-1' boundary conditions :- (a)-(d): Distribution of Peclet number for droplets of different initial diameter; for each initial diameter, Peclet number data along 400 paths is obtained and plotted. (e): Plot showing spread of Peclet number for different initial diameter

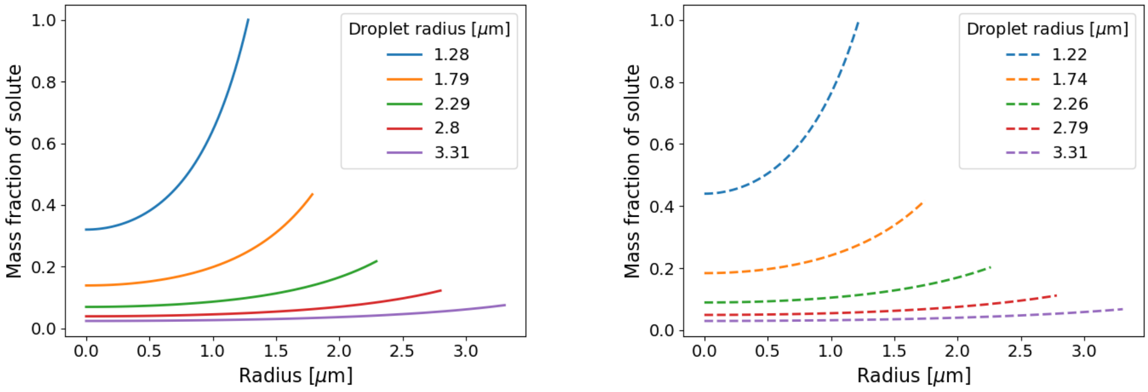

(a) At high drying rate for initial diameter = 6.6 μm

(b) At low drying rate for initial diameter = 6.6 μm

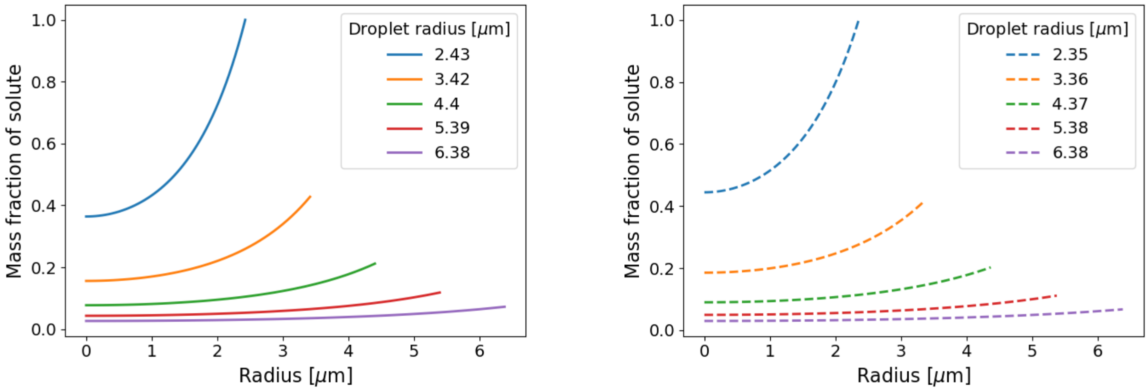

(c) At high drying rate for initial diameter = 12.8 μm

(d) At low drying rate for initial diameter = 12.8 μm

Figure 5.10: Solute concentration as a function of radius at high and low drying rate for droplets of initial diameter 6.6 μm and 12.8 μm (obtained from simulations of 'Case-1' boundary conditions).

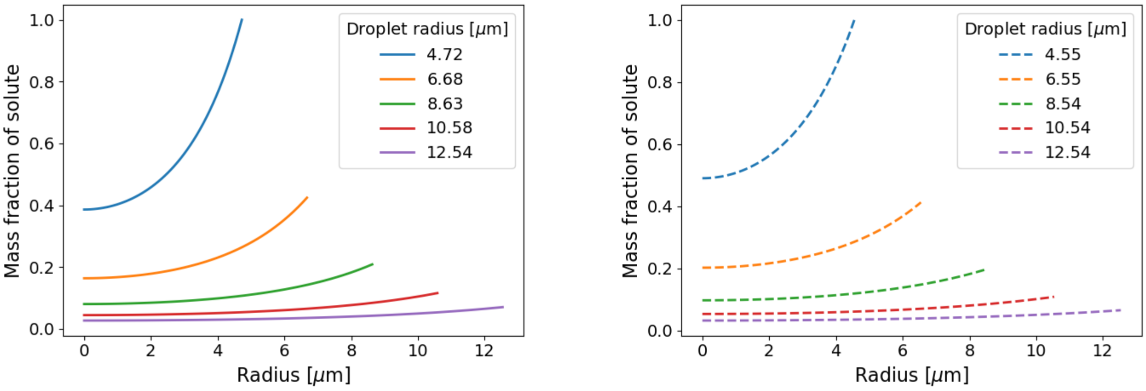

(a) At high drying rate for initial diameter = 25.1 μm

(b) At low drying rate for initial diameter = 25.1 μm

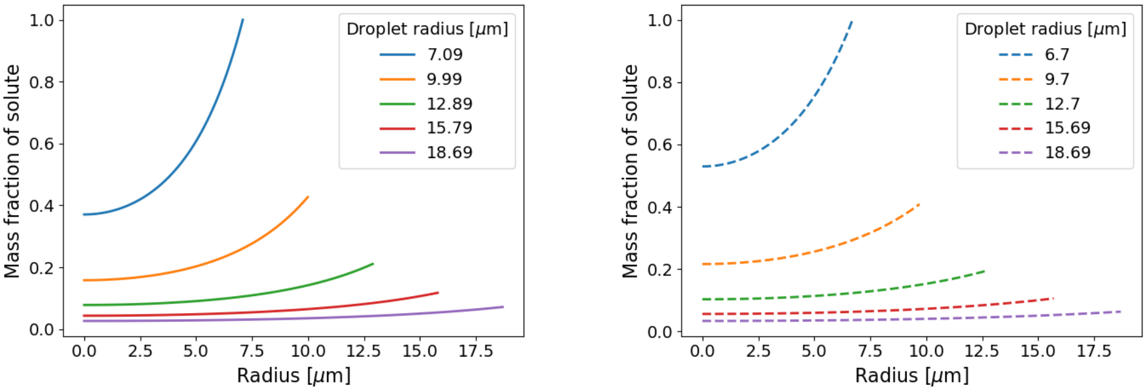

(c) At high drying rate for initial diameter = 37.4 μm

(d) At low drying rate for initial diameter = 37.4 μm

Figure 5.11: Solute concentration as a function of radius at high and low drying rate for droplets of initial diameter 25.1 μm and 37.4 μm (obtained from simulations of 'Case-1' boundary conditions).

The multiphase simulations are run for the ’Case-2’ boundary conditions as well and the corresponding drying data is analysed for the same set of initial diameters. The ’Case-2’ boundary conditions reflect different set of process operating conditions when compared with ’Case-1’. In ’Case-2’, the impact of increased solution flow rate, while maintaining the same exhaust temperature as in ’Case-1’, is analysed. It is important to maintain a certain value of exhaust temperature as it influences stickiness of the powder, moisture content of the particles and stability of the components in the particle. It is worth mentioning that the different process condition parameters in a spray dryer system are constrained with each other. Thus, keeping the exhaust temperature constant and increasing the solution flow rate eventually leads to an increase in drying gas inlet temperature. The ’Case-2’ boundary conditions are detailed in Table 4.7.

The mean rate and mean Peclet number for droplets of different initial diameter for both the cases is plotted as shown in Figure 5.12. It is expected that with an increase in drying gas inlet temperature in ’Case-2’, there will be an increase in drying rate and corresponding Peclet number. However, there is also an increase in solution mass flow rate, which translates to an increased amount of water in the injected solution. Hence, the drying rate is lower in ’Case-2’ when compared with ’Case-1’. The reason for this can be found by looking at the relative humidity contour plots. The relative humidity of the continuous phase determines the gradient that drives the drying process. It is worth recalling that the relative humidity is the ratio of the partial pressure of water vapour in the mixture to the equilibrium pressure of water at a given temperature. The drying rate is described by Equation 3.1, where the effect of the relative humidity is represented as the term $C_{v,\infty}$ which is a function of the partial pressure of water vapour and the temperature of the continuous phase. As is evident from Figure 5.13, the relative humidity of the continuous phase is higher in ’Case-2’ compared with ’Case-1’. Hence, the gradient driving the mass transfer is lower in ’Case-2’ resulting in lower drying rates as compared with ’Case-1’. The same is better illustrated in particle tracks. The particle tracks shown in Figure 5.14 are coloured based on relative humidity and the particle paths just before the particles completely dry out are shown. It can be seen that the particles in ’Case-2’ experience higher relative humidity of the continuous phase when compared to that in ’Case-1’. This indicates the impact of changing process conditions, especially increased mass flow rate of solution, on the drying rate and Peclet number, and hence, the corresponding particle structure. Therefore, these results agree with the observations that show the relevance of solvent activity, over the impact of drying gas inlet temperature or exhaust temperature, on the particle structure [24]. However, as is evident from the overlap of distribution of drying rates (and Peclet numbers) of the two cases, this impact of process conditions on particle structure may not be easily identifiable by the available particle characterization techniques.

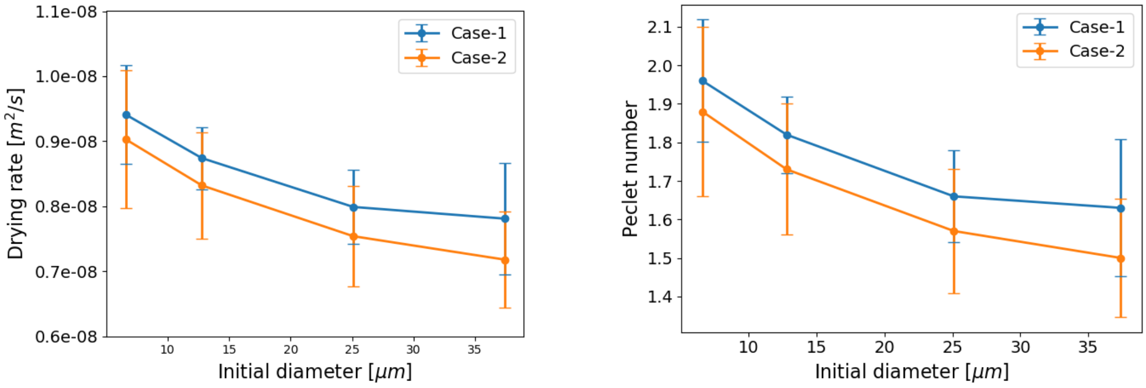

(a) Drying rate vs initial diameter

(b) Peclet number vs initial diameter

Figure 5.12: Comparison of results obtained from simulations with 'Case-1' and 'Case-2' boundary conditions (as detailed in subsubsection 4.1.3.3).

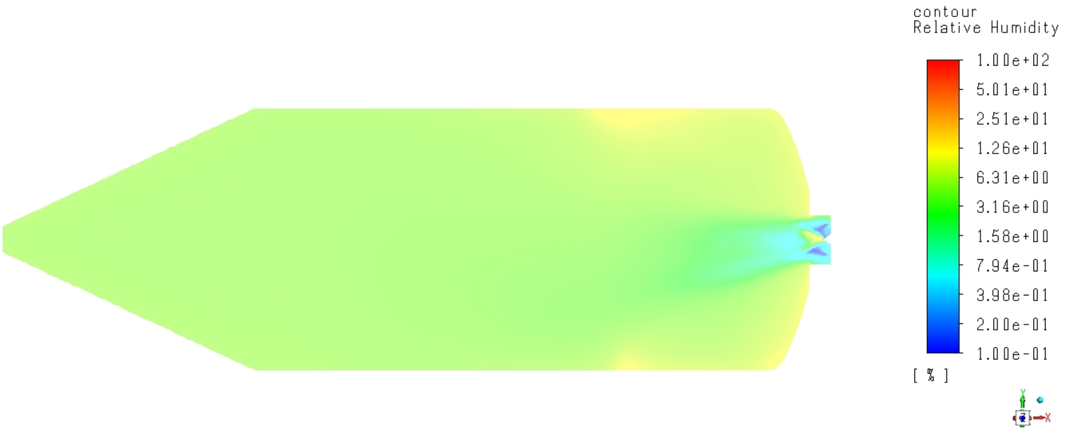

(a) 'Case-1'

(b) 'Case-2'

Figure 5.13: Contour plot of relative humidity of continuous phase

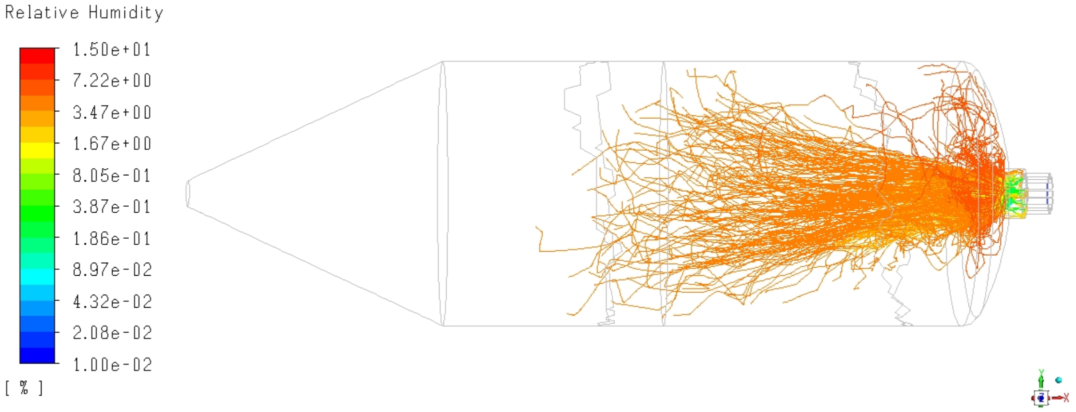

(a) 'Case-1'

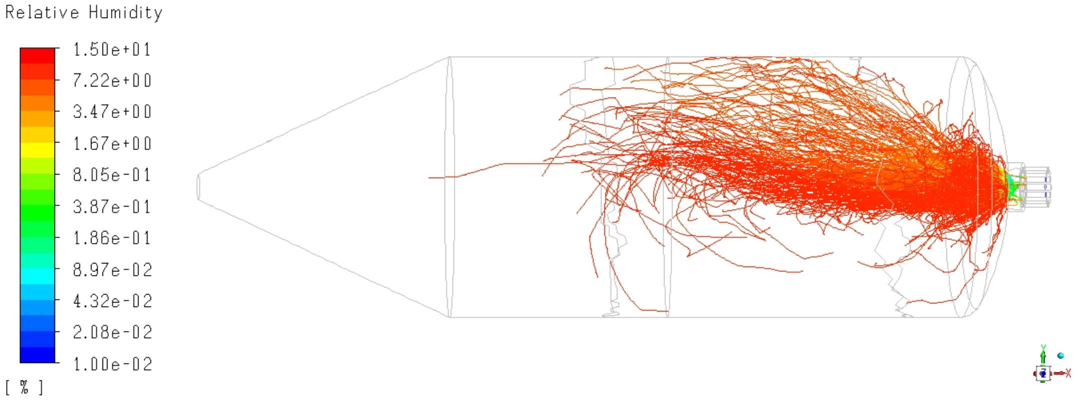

(b) 'Case-2'

Figure 5.14: Tracks of discrete phase coloured based on relative humidity of continuous phase

6

Conclusion

In this thesis, a 3D simulation model for the 'Anhydro MicraSpray 35' spray dryer is developed. Drying in the main dryer is influenced by the flow in components upstream of the main dryer body, such as the drying gas chamber and the atomizer. Hence, these components are also modeled to ensure the right boundary conditions. The multiphase flow in the dryer is modelled using an Eulerian-Lagrangian approach. The different model parameters selected based upon sensitivity analysis lay the foundation of the developed framework. The drying data for two different operating conditions is analysed.

Analysis of the drying data obtained from the simulation reveals that the rate of drying of droplets of same initial diameter is different since they follow different trajectories, and hence, a range of drying rate for droplets of same initial diameter is obtained. A range of drying rate translates to a corresponding variation in structure and composition of final particles obtained from droplets with same initial diameter. Analysis of drying data for the case with increased solution flow rate reveals a decrease in mean drying rate and Peclet number. This is due to an increase in solvent activity in the continuous phase resulting from an increased solvent content in the injected solution. This indicates the impact of process conditions, especially the mass flow rate of the solution, on the drying rate, and hence, the corresponding particle structure. Therefore, these results agree with the observations that show the relevance of solvent activity, over the impact of drying gas inlet temperature or exhaust temperature, on the particle structure [24]. However, as is evident from the overlap of distribution of drying rate of the two cases, this impact of process conditions on particle structure may not be easily identifiable by the available particle characterization techniques.

There are a few things that will surely increase the reliability of the model. In future work, transient simulation for the continuous phase will be better representative of the flow field in the dryer. Validating the simulation results at different stages against experimental data will bring more confidence in the quantitative results. The simulation methodology in this thesis does not include the second-stage of drying which will be representative of the complete physics of the drying process and therefore, could be included in future work.

Bibliography

[1] Maksim Mezhericher, Avi Levy and Irene Borde. *Multi-Scale Multiphase Modeling of Transport Phenomena in Spray-Drying Processes.* Drying Technology, 33:1, 2015.

[2] Sadegh Poozesh and Ecevit Bilgili. *Scale-up of pharmaceutical spray drying using scale-up rules: A review.* International Journal of Pharmaceutics, 2019.

[3] Asep Bayu Dani Nandiyanto, Kikuo Okuyama. *Progress in developing spray-drying methods for the production of controlled morphology particles: From the nanometer to submicrometer size ranges.* Advanced Powder Technology, 2011.

[4] Herm E. Snyder, David Lechuga-Ballesteros. *Spray Drying: Theory and Pharmaceutical Applications.* Pharmaceutical Dosage Forms - Tablets Vol. 1, 2008, p 227-260.

[5] Rainer Bellinghausen. *Spray drying from yesterday to tomorrow: An industrial perspective.* Drying Technology, 2019.

[6] Ahmad Ziaee, et. al., *Spray drying of pharmaceuticals and biopharmaceuticals: Critical parameters and experimental process optimization approaches.* European Journal of Pharmaceutical Sciences, 2018

[7] Kamlesh Patel, Xiao Dong Chen, Romain Jeantet, Pierre Schuck. *One-dimensional simulation of co-current, dairy spray drying systems – pros and cons.* Dairy Science & Technology, 2010.

[8] Mark Pinto, Ian Kemp, Sean Bermingham, Thoralf Hartwig, Ariane Bisten. *Development of an axisymmetric population balance model for spray drying and validation against experimental data and CFD simulations.* Chemical Engineering Research and Design, 2014.

[9] Reinhard Vehring, Willard R. Foss, David Lechuga-Ballesteros. *Particle formation in spray drying.* Journal of Aerosol Science, 2007.

[10] Stefan Blei, Martin Sommerfeld. *CFD in Drying Technology- Spray Dryer Simulation.* Modern Drying Technology Vol. 1, 2014.

[11] Mariano Martín, Mario R. Eden, Nishanth G. Chemmangattuvalappil. *Tools For Chemical Product Design - From Consumer Products to Biomedicine.* Elsevier, 2017, p 509-579.

[12] Eline Boel, et. al., *Unraveling Particle Formation: From Single Droplet Drying to Spray Drying and Electrospraying.* Pharmaceutics, 2020.

[13] Muzammil Ali, et. al., *A one-dimensional plug-flow model of a counter-current spray drying tower.* Chemical Engineering Research and Design, 2014.

[14] Maksim Mezhericher, Avi Levy and Irene Borde. *The Influence of Thermal Radiation on Drying of Single Droplet/Wet Particle.* Drying Technology, 2008

[15] W. E. Ranz, W. R. Marshall. *Evaporation from drops.* Chemical Engineering Progress, 1952.

[16] S. A. Morsi, A. J. Alexander. *An investigation of particle trajectories in two-phase flow systems.* Journal of Fluid Mechanics, 1972.

[17] Clayton T. Crowe, John D. Schwarzkopf, Martin Sommerfeld, Yutaka Tsuji. *Multiphase flows with droplets and particles.* CRC Press LLC, 2012.

[18] Hamid Reza Norouzi, Reza Zarghami, Rahmat Sotudeh-Gharebagh, Navid Mostoufi. *Coupled CFD-DEM Modeling: Formulation, Implementation and Applications to Multiphase Flows.* John Wiley & Sons, 2016.

[19] T. A. G. Langrish, D. F. Fletcher. *Spray drying of food ingredients and applications of CFD in spray drying.* Chemical Engineering and Processing 40, 2001.

[20] Bengt Andersson, et. al., *Computational Fluid Dynamics for Engineers.* Cambridge University Press, 2018.

[21] *ANSYS Fluent User's Guide. 2019 R3, ANSYS Inc.*

[22] Tatsuya Umecky, et. al., *Binary Diffusion Coefficients of Aqueous Phenylalanine, Tyrosine Isomers, and Aminobutyric Acids at Infinitesimal Concentration and Temperatures from (293.2 to 333.2) K.* Journal of Chemical and Engineering Data, 2013.

[23] Youguang Ma, Chunying Zhu, Peisheng Ma, K. T. Yu. *Studies on the Diffusion Coefficients of Amino Acids in Aqueous Solutions.* Journal of Chemical and Engineering Data, 2005.

[24] Allen C. Templeton, et. al., *Discovering and Developing Molecules with Optimal Drug-Like Properties* Springer, 2015, p 383-434.

A

Appendix

A.1 Phase coupling parameter estimation

The momentum coupling parameter can be estimated from [17]:

$$\Pi_{mom} = \frac{Z}{1 + St_{mom}} \tag{A.1}$$

$$St_{mom} = \frac{\tau_v}{\tau_f} \tag{A.2}$$

where the particle relaxation time (τ_v) is given by:

$$\tau_v = \frac{\rho_p d_p^2}{18\mu_c} \tag{A.3}$$

The characteristic time of the flow field (τ_f) for the current system is 4 sec. For a droplet density of 1018 kg/m^3, a fluid viscosity of 6.88 x 10^{-6} kg/ms and considering the largest diameter of 43.53 μm in the droplet size distribution as the worst case, the momentum coupling parameter (Π_{mom}) was calculated to be 0.009.

The value of mass coupling parameter can be estimated from [17]:

$$\Pi_{mass} = \frac{Z}{St_{mass}} \tag{A.4}$$

$$St_{mass} = \frac{\tau_m}{\tau_f} \tag{A.5}$$

The characteristic evaporation time (τ_m) can be estimated from:

$$\tau_m = \frac{d_{p,o}^2}{\kappa} \tag{A.6}$$

$$\kappa = \frac{4Sh\rho_c D_A}{\rho_p}(\omega_{A,s} - \omega_{A,\infty}) \tag{A.7}$$

Here, Z denotes loading and is given by the ratio of overall mass flow rate of dispersed phase to that of the continuous phase and for the current system is given by 0.42 kg/hr and 43.14 kg/hr, respectively.

For Sh $\sim$ 2, a gas phase density of 1.2 kg/m^3, a diffusion co-efficient (D_A) of 3.59 x 10^{-5} m^2/s for water-vapour in nitrogen, a mass fraction of water at the surface

($\omega_{A,s}$) of 0.95 and zero mass fraction of water in the free stream ($\omega_{A,\infty}$), the mass coupling parameter for an initial droplet size of 43.53 μm was calculated to be 6.

The value of energy coupling parameter can be estimated from [17]:

$$\Pi_{energy} = \frac{Z}{St_{mass}} \frac{h_{lat}}{c_{p,c}T_c} \tag{A.8}$$

With the values of 2263 kJ/kg for the latent heat of evaporation of water (h_{lat}), 1042 J/kg/K for the specific heat capacity of continuous phase ($c_{p,c}$) and an inlet temperature of the continuous phase (T_c) to be 385 K, the energy coupling parameter was estimated to be 35.

A.2 Volume fraction of dispersed phase

The volume fraction of the dispersed phase is defined as:

$$\alpha_d = \lim_{\delta V \to \delta V_o} \left(\frac{\delta V_d}{\delta V}\right) \tag{A.9}$$

To estimate volume fraction of the dispersed phase close to the injection point, the size of the averaging volume is taken to be the volume of a computational cell. Therefore, V_d is calculated as:

$$V_d = Q_d * \tau_{r,max} \tag{A.10}$$

where Q_d is the volumetric flow rate of the dispersed phase and $\tau_{r,max}$ is the maximum residence time, considering the worst case, and is calculated as:

$$\tau_{r,max} = \frac{cell\, dimension(m)}{u_{min}(m/s)} \tag{A.11}$$

The average cell dimension in the injection region is 0.002 m and the minimum velocity of the discrete phase in that region is obtained from the continuous phase velocity and considering that the particles completely follow the continuous phase, gives:

$$u_{min} = 37 m/s \tag{A.12}$$

Thus, $\tau_{r,max}$ is calculated to be 5.4 x 10^{-5} s and substituting for Q_d as 1.167 x 10^{-7} m^3/s in Equation A.10 gives:

$$V_d = 6.31 \times 10^{-12}\, m^3 \tag{A.13}$$

The denominator in Equation 3.21 is the volume of the computational cell. For a tetrahedron with an edge of 0.002 m, the volume is estimated from:

$$V_{cell} = \frac{a^3}{6\sqrt{2}} = 9.43 \times 10^{-10}\, m^3 \tag{A.14}$$

The resulting volume fraction very close to the injection point is:

$$\alpha_{d,max} = \frac{V_d}{V_{cell}} \tag{A.15}$$

$$\alpha_{d,max} = \frac{6.31 \times 10^{-12}}{9.43 \times 10^{-10}} = 0.006 \tag{A.16}$$

However, in regions far from the injection point, the volume fraction is much smaller than that estimated here, as can be seen from the contour plot below.

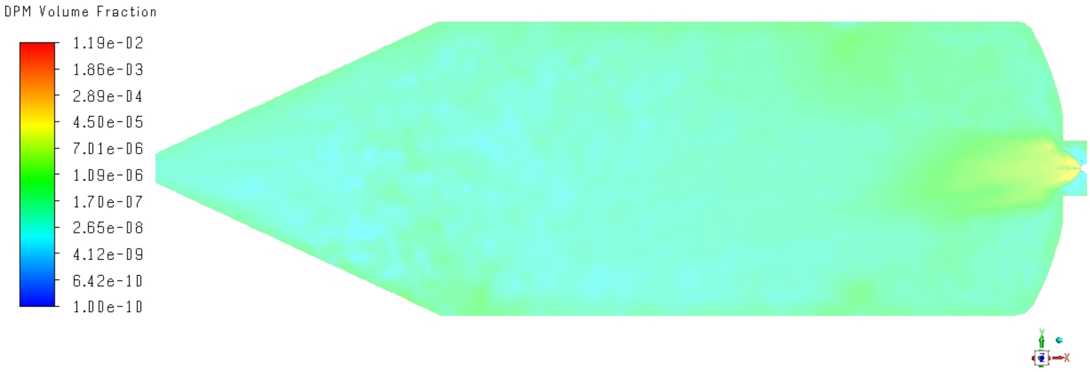

Figure A.1: Contour plot of volume fraction of the discrete phase.

A.3 Estimation of solute concentration in the particle

The distribution of chemical components in an evaporating droplet is given by:

$$\frac{\partial c_i}{\partial t} = \frac{D_i}{r_s^2}\left(\frac{\partial^2 c_i}{\partial R^2} + \frac{2\partial c_i}{R\partial R}\right) + \frac{R\partial C_i \partial r_s}{r_s \partial R \partial t} \tag{A.17}$$

where c_i denotes concentration of solute i, D_i the diffusion coefficient of solute i in the liquid phase, r_s is the droplet radius and $R = r/r_s$ is the normalized radial coordinate. The above equation is based on the assumption of constant diffusion coefficient and absence of internal convection in the droplet.

The Equation A.17 has an analytical solution under steady-state condition. A constant evaporation rate fulfills the steady state condition as given by:

$$\frac{\partial d^2}{\partial t} = -\kappa = 8 r_s \frac{\partial r_s}{\partial t} \tag{A.18}$$

where d is the droplet diameter and κ is the evaporation rate.

The solution to Equation A.17 under the assumption of constant evaporation is given by:

$$c_i = c_{c,i} exp\left(-\frac{r_s \partial r_s}{2D_i \partial t} R^2\right) \tag{A.19}$$

where $c_{c,i}$ is the concentration of solute i at the center of the droplet.

It is more useful to express the concentration as a function of the average concentration, c_m, because of the ease of its calculation using a simple mass balance. Thus, expressing Equation A.19 as a function of the average concentration yields:

$$c_i = c_{m,i} \frac{exp(Pe_i R^2/2)}{3\int_0^1 R^2 exp(Pe_i R^2/2) dR} \tag{A.20}$$

Here the dimensionless Peclet number, Pe, is given by:

$$Pe_i = -\frac{r_s \partial r_s}{D_i \partial t} = \frac{\kappa}{8D_i} \tag{A.21}$$

For $R = 1$, the surface concentration can be found as:

$$\begin{aligned} c_{s,i} &= \frac{c_{m,i}}{3\beta_i} exp\left(\frac{Pe_i}{2}\right) \\ \text{with} \quad \beta_i &= \int_0^1 R^2 exp(Pe_i R^2/2) dR \end{aligned} \tag{A.22}$$

To estimate β, an approximate expression for the surface enrichment, E_i can be used and is given by:

$$E_i = \frac{c_{s,i}}{c_{m,i}} = 1 + \frac{Pe_i}{5} + \frac{Pe_i^2}{100} - \frac{Pe_i^3}{4000} \tag{A.23}$$

Thus, through Equation A.23, we obtain the value for $c_{s,i}/c_{m,i}$ and substituting for this in Equation A.22, we obtain the value for β. Substituting for β in Equation A.20, we can obtain concentration of solute as a function of droplet radius.